



Elucidating metal composition–coking relationships and coke formation pathways during gas-phase oxydehydration of glycerol over clay mineral-supported Mo-V-O catalysts

Alfin Kurniawan ^{a,b}, Shu Tian Yin ^{a,c}, Da Jian Li ^{a,c}, Ke Jin Li ^a, Xiao Lan Chen ^{a,c}, Wei Jun Huang ^a, Peng Yang Zhao ^a, Jia Hui Liu ^a, Chun Hui Zhou ^{a,b,c,*}

^a Research Group for Advanced Materials & Sustainable Catalysis (AMSC), State Key Laboratory of Green Chemistry Synthesis Technology, College of Chemical Engineering, Zhejiang University of Technology, Hangzhou 310032, China

^b Anhui International Exchange and Cooperation Base, Qing Yang Institute for Industrial Minerals, Youhua, Qingyang, Anhui 242804, China

^c Engineering Research Center of Non-metallic Minerals of Zhejiang Province, Zhejiang Institute of Geology and Mineral Resource, Hangzhou 310007, China



ARTICLE INFO

Keywords:

Glycerol
Oxydehydration
Coke
Polycyclic aromatic compounds
Catalyst deactivation
Molybdenum-vanadium

ABSTRACT

Catalyst deactivation by carbon deposition (coking) remains a major obstacle in many important industrial processes, such as catalytic gas-phase oxydehydration of glycerol. Understanding the chemical nature and development of coke species during the time-on-stream (TOS) of the catalytic solids is therefore crucial for mitigating the extent of coking and in the design of regeneration process of the coked catalysts. In this study, multiple analytical techniques, including SEM, XRD, FTIR, Raman, GC-MS, XPS, and ¹³C solid-state MAS NMR were employed to gain insights into the coking behavior of acid-activated montmorillonite (HMMT) supported Mo-V-O catalysts with modulated metal ratios, along with soluble and insoluble coke compositions and their evolution over time. Insoluble coke was comprised of polycyclic aromatic compounds with 5 or more fused-benzene rings containing different types of oxygen-bonded groups, such as –OCH₃, –COOH, –CHO, and –OH. The major chemical constituents of soluble coke were mononuclear aromatic derivatives (i.e., xylenes, 2,4-di-tert-butylphenol, and 1-hydroxycyclohexyl phenyl ketone) and paraffinic hydrocarbons with 12–18 carbon atoms. The latter coke species is thought to be formed via the deoxygenation of linear oligoglycerols. The insights presented in this study may aid in understanding the carbon deposition process during gas-phase oxydehydration of glycerol for improved design of supported Mo-V-O catalyst materials with high coking resistance.

1. Introduction

The large surplus of glycerol byproduct (~10 wt%) generated from the biodiesel industry (a global amount of ca. 3.8 million metric tons in 2021 [1]) has created a tremendous opportunity to advance sustainable production of important commodity chemicals from this low-value renewable feedstock, such as acrolein, propanediols, lactic acid, acetins, etc. [2–6]. From an industrial perspective, the Brønsted acid-catalyzed gas-phase dehydration of glycerol represents one of the most attractive conversion routes for manufacturing acrolein, an important chemical intermediate used in the production of acrylic acid, acrylate monomers, methionine, detergents, and polymers. Acrylic acid can also be co-produced with acrolein in a one-pot process through a

dehydration-oxidation reaction over acid–metal bifunctional catalysts [7]. Typical solid acid materials for catalyzing glycerol dehydration to acrolein include zeolites, metal oxides, supported heteropolyacids, and clay minerals [7], while V-containing mixed metal oxides (e.g., V-Mo-O, V-W-O, V-Mo-Cu-O, and V-W-Nb-O) have been reported to be active and selective in the partial oxidation of acrolein to acrylic acid [8–11]. Montmorillonite (MMT), a low-cost, ubiquitous, and important industrial clay mineral, is especially attractive and shows promise either as a support material or dehydration catalyst [12–14], owing to its abundant acidic catalytic sites. As a particular example, MMT-supported WO_x catalyst containing tunable acid and metal sites exhibit good catalytic activity in the gas-phase dehydration of glycerol with ~90% conversion and ~82% selectivity to acrolein at 320 °C [12]. However, similar to

* Corresponding author at: Research Group for Advanced Materials & Sustainable Catalysis (AMSC), State Key Laboratory of Green Chemistry Synthesis Technology, College of Chemical Engineering, Zhejiang University of Technology, Hangzhou 310032, China.

E-mail address: clay@zjut.edu.cn (C.H. Zhou).

other solid acids mentioned earlier, MMT-based catalysts deactivate with time-on-stream (TOS) due to progressive deposition of carbonaceous compounds. In this context, the carbon deposits (coke) either cover the acidic active sites of the catalyst responsible for the formation of acrolein or block pores that hinder the diffusion of reactant and product species into and out of the catalyst [15,16], which necessitates high-temperature oxidative treatment to liberate the coke and thereby restore the catalytic activity. Indeed, to improve the long-term catalyst performance, lower the operational cost for regeneration and, more importantly, to provide a rationale for design of coke-resistant catalysts, detailed insights into the coke characteristics, such as the changes in morphology and/or chemical composition over TOS, and coke-forming reactions during gas-phase glycerol oxydehydration are needed, in particular for industrially relevant MMT-supported mixed metal oxide catalysts.

Coking of catalysts during gas-phase oxydehydration of glycerol is a complex process that involves numerous parallel and consecutive reactions between various oxygenate products [17,18]. Within this context, the so-called “dual oxygenate and hydrocarbon pools” mechanism has been proposed to explain the formation of olefinic and aromatic coke precursors, respectively [19]. According to this mechanism, short-chain olefins (C₂–C₄) may be formed by deoxygenation of acetone and the C=O bond dissociation of acetaldehyde, whereas monoaromatic compounds (C₆–C₉) are produced either via the aldol condensation, dehydration, and aromatization of C₂–C₃ oxygenates or cracking of heavier aromatics in the hydrocarbon pool. The formed olefin and aromatic species can further react themselves or with each other to produce higher molecular weight molecules that contribute to coking. In addition, the reactant itself (glycerol) is considered as a potential coke precursor during the catalytic reaction, which can undergo oligomerization and cyclization reactions to form polyglycerols and branched polyols (polyglycols), respectively [20]. Obviously, the amount of deposited coke and the coking rate are strongly dependent on both the catalyst characteristics (e.g., pore structures, crystallinity, and surface acidity including type and strength of the acidic sites) and operating conditions, such as reaction temperature, glycerol feed concentration, space velocity, and TOS [17,18,21–24]. For example, Suprun et al. [17] showed that the coke formation is more prominent for microporous catalysts possessing narrow pores and higher surface acidity. In line with this, Kim et al. [22] and Vieira et al. [23] reported that solid catalysts containing higher strong Brønsted acid site concentrations coke more severely than those with weak acidity and hence exhibit poorer TOS stability. Regarding the effects of reaction conditions, Corma and coworkers [18] found that lower temperature and space velocity (or higher catalyst-to-feed ratio) favoring acrolein selectivity concomitantly lead to higher coke yields. They also found that the use of high-concentration aqueous glycerol feeds promotes the formation of coke via hydrogen transfer reactions of products, in agreement with the work of Kim et al. [22]. While all these studies have shed light on the correlation between the textural and acidic properties of the catalyst and the coke yield under various reaction conditions, little is known about the structure, composition, and evolution pathway of coke. Moreover, although the nature of coke formed on the catalyst towards the end of the reaction has been commonly attributed to large polycyclic aromatic structures (or polycyclic aromatic hydrocarbons) in prior studies, the mechanism of how this molecular entity is formed from smaller aromatic molecules and/or reactive intermediate species with increasing TOS during gas-phase glycerol oxydehydration remains poorly understood. Likewise, the deposited coke is thought to be composed of soluble (light) and insoluble (heavy) constituents similar to those observed in the methanol-to-olefins [25] and ethylene-to-aromatics [26] conversions, and their formation with TOS may follow distinct mechanisms.

Despite immense challenges in elucidating the structure and chemical identity of coke with reaction progress, there have been a few studies performing multitechnique characterization of the coked catalysts. The chemical nature of the coke deposits has been examined using

spectroscopic methods, such as ultraviolet-visible (UV-vis) [27], UV-Raman [28], Fourier transform infrared (FTIR) [26], and ¹³C magic-angle spinning nuclear magnetic resonance (MAS NMR) [23,25,29]. However, the direct identification of the molecular structure of coke by these spectroscopic techniques has proven difficult due to the complexity of organic compounds, in particular for insoluble polycondensed aromatic coke [25]. Meanwhile, the characterization of spent catalysts by electron microscopy and X-ray diffraction (XRD) techniques can provide only information on the structural features of carbon deposits, and therefore needs to be complemented by spectroscopic analysis to obtain a detailed picture of the nature of coke species. Hitherto, such multitechnique characterization studies of spent catalysts to provide insights into the coke formation mechanisms have been only demonstrated for methanol-to-olefins processes on zeolites, while no example has been reported for gas-phase oxydehydration of glycerol. In addition, the quantitative relationships between metal composition and the coking tendency in supported Mo-V oxide catalysts, an industrially relevant material employed in this process, are lacking.

In the present contribution, we investigate the catalytic performance and the coking deactivation of composition-tuned Mo-V loaded acid-treated MMT catalysts (Mo-V/HMMT) in the gas-phase oxydehydration of glycerol as a model coke-forming reaction, with the main focus on determining the nature of the coke deposits (i.e., structure and composition) and potential reaction routes. To accomplish this goal, the coking process on the catalyst surface was evaluated at different TOS and correlated with the product distributions of the deactivated catalysts. Indeed, to better understand the coke composition and its temporal evolution during the reaction, the soluble components of bulk coke molecules were isolated by solvent extraction and characterized separately by gas chromatography-mass spectrometry (GC-MS) to quantify the distribution and contents of organics. Meanwhile, the retained insoluble coke species on the catalyst surface were examined using a combination of ¹³C solid-state MAS NMR and X-ray photoelectron spectroscopy (XPS) techniques. Along with other characterization tools, including scanning electron microscopy (SEM), X-ray diffraction (XRD), and Raman spectroscopy, the structural and chemical nature of soluble and insoluble coke compounds, and their formation mechanisms during glycerol oxydehydration have been successfully determined. To the best of our knowledge, a detailed study of the composition-dependent coking over Mo-V/HMMT catalysts and insights into the reaction mechanism for gas-phase oxydehydration of glycerol has not been previously reported in the literature. The present finding may contribute to a better understanding of the coking process taking place during the oxydehydration of glycerol and is expected to benefit future design strategies of low-cost mineral supported multimetal oxide catalysts with improved coke resistance for advancing sustainable industrialization of glycerol-to-acrolein/acrylic acid conversion processes.

2. Experimental

2.1. Materials

Raw Na-MMT was obtained from Anhui Province, China and used after further purification. Glycerol (99%) was purchased from Sigma-Aldrich and used as received without further purification. Ammonium molybdate tetrahydrate ((NH₄)₆Mo₇O₂₄·4 H₂O, ≥ 99%) and ammonium metavanadate (NH₄VO₃, 99%) were used as precursors for Mo and V metals, respectively. All aqueous solutions were prepared using deionized (DI) water.

2.2. Catalyst preparation

2.2.1. Preparation of acid-activated MMT

Na-MMT powders were dispersed in an aqueous phosphoric acid solution (1 M) to prepare a 5 wt% suspension. The activation process was carried out in a round-bottomed flask fitted with a reflux condenser

under vigorous stirring for 4 h at 80 °C. Afterward, the solid was collected by centrifugation and washed with DI water repeatedly until the pH of the filtrate became around 7, dried at 80 °C for 24 h, and finally ground to fine powders. The acid-activated MMT was denoted as HMMT throughout the manuscript. To study the influence of support acidity on the catalytic and coking activity of Mo-V/HMMT catalysts, 0.5 and 2.0 M aqueous H₃PO₄ solutions were also used during modification of MMT and the obtained materials were designated as 0.5HMMT and 2HMMT, respectively.

2.2.2. Preparation of bifunctional Mo-V/HMMT catalysts

Mo-V/HMMT catalysts were prepared by an incipient wetness impregnation method following previously reported procedure with some modifications [30]. The total loading mass of Mo and V was fixed at 5 wt%, while the nominal mole ratios of Mo/(Mo+V) were varied from 0.4 to 0.8. In a typical preparation of Mo-VHMMT catalyst with a 0.8 Mo/(Mo+V) ratio, 0.0146 g of NH₄VO₃ (0.125 mmol) and 0.0904 g of (NH₄)₆Mo₇N₆O₂₄·4 H₂O (0.073 mmol) were dissolved in 20 mL of DI water at 60 °C under stirring. Then, 2 g of HMMT was added to the aqueous bimetal precursor solution and the mixture was stirred for 5 h, followed by aging at this temperature overnight. Later, the sample was dried at 80 °C for 12 h and subsequently calcined in air at 500 °C for 4 h. The Mo-V/HMMT catalysts with nominal Mo/(Mo+V) mole ratios of 0.4 and 0.6 were also synthesized using the same procedure as described above, but with different amounts of Mo and V metal precursors. In addition, single metal-loaded HMMT catalysts (i.e., Mo/HMMT and V/HMMT) with a nominal metal loading of 5 wt% were prepared to investigate the relationship between metal compositions and the catalytic activity and coking behavior during the TOS reaction, as well as to correlate the results with those of Mo-V/HMMT catalysts.

2.3. Catalytic tests

The gas-phase glycerol oxydehydration was carried out in a continuous downflow fixed-bed quartz reactor (52 cm long, 2 cm outer diameter, and 1 cm inner diameter) at atmospheric pressure and 320 °C (see Figure S1 for details). Typically, 0.5 g of catalyst (60–80 mesh) was packed between quartz sands (20–40 mesh) within the isothermal zone of the reactor (10 cm) and retained by quartz wool below the catalyst bed. Prior to the catalytic tests, the assembled catalyst bed was first pretreated in flowing air (21 mL/min) at target reaction temperature for 30 min. Subsequently, a 20 wt% aqueous glycerol solution was fed into the vaporizer (180 °C) at a flow rate of 0.10 mL/min by a Kontron Instruments 422 HPLC pump and the vaporized feed was swept through the reactor using air as carrier gas at 21 mL/min. The glycerol weight hourly space velocity (WHSV) was 2.51 h⁻¹ accordingly. The condensable organic products leaving the reactor were collected hourly in a gas-liquid separator at 3 °C for 5 h on stream and analyzed offline by a gas chromatograph (Shimadzu GC-2014) equipped with an AT-FFAP capillary column (30 m length, 0.32 mm internal diameter, and 0.25 µm film thickness) and a flame ionization detector. The GC analysis of the liquid samples was used to evaluate the yield and product composition. The non-condensable gaseous products and the carbon deposits formed on the catalyst during the reaction were denoted by “others” to maintain the mass balance. The glycerol conversion (X) and product selectivity (S) were calculated using Eqs. (1) and (2), respectively:

$$X = \frac{\text{Moles of glycerol reacted}}{\text{Moles of glycerol fed into the reactor}} \times 100\% \quad (1)$$

$$S = \frac{\text{Moles of glycerol converted to a specific product}}{\text{Moles of glycerol reacted}} \times 100\% \quad (2)$$

2.4. Extraction of soluble coke components

The chemical nature of the coke deposits formed over Mo-V/HMMT

catalysts at different TOS experiments was thoroughly investigated by first separating its soluble and insoluble fractions. Typically, 0.2 g of spent catalyst from the reaction was sieved at 60 mesh to separate quartz sand and then mixed with 10 mL tetrachloromethane (CCl₄). Compared to methylene chloride (CH₂Cl₂) employed in the Guisnet method [15], the use of CCl₄ as a solvent could allow for more efficient separation of soluble organic components from bulk coke deposits on the surface [25]. The carbon species dissolved in CCl₄ was labeled as soluble coke. The catalyst and coke species remaining after this process (denoted as insoluble coke) were then recovered by filtration, washed with acetone, and dried at 60 °C for 2 h. Note that in the conventional Guisnet approach for characterization of coke components, the coked catalyst was subjected to digestion by treating with a 40% hydrofluoric acid solution prior to extraction. This process, however, destroys the whole structure of the catalyst, thus making it impossible to obtain useful information regarding the location of carbon deposits and pore blocking within the catalyst body during the TOS reaction. Hence, in the present experiments, instead of using such a destructive approach, the spent catalysts were treated with CCl₄ for a prolonged duration to maximize the extraction of external/surface and internal soluble coke species.

2.5. Characterizations of spent catalysts and coke species

Powder XRD patterns were obtained using a PANalytical X'Pert PRO diffractometer (40 kV, 40 mA) between 2° and 80° (2θ) with a scanning rate of 0.1°/s using Ni-filtered Cu Kα radiation (λ = 0.1541 nm) as the X-ray source.

N₂ physisorption isotherms were measured at –196 °C on a Micromeritics ASAP2020 instrument. Before analysis, the samples were degassed in vacuo at 200 °C for 12 h. The BET method was employed to determine the specific surface area of the samples, whereas the total pore volume (V_T) was taken from the volume adsorbed at a relative pressure (P/P₀) of 0.995. The average pore diameter (4 V/A) and pore size distribution (PSD) were calculated by the Barrett-Joyner-Halenda (BJH) method from desorption branch of the isotherms.

Transmission FTIR spectra were recorded at room temperature on a Nicolet 6700 spectrometer in the 400–4000 cm⁻¹ region with a resolution of 4 cm⁻¹. Samples were prepared as pressed KBr pellets. Attenuated total reflection FTIR (ATR-FTIR) measurements were performed on a Thermo Nicolet iS50 spectrometer equipped with a diamond crystal module by acquiring 64 scans at a 4 cm⁻¹ resolution from 4000 to 400 cm⁻¹. Before analysis, all catalyst samples were gently ground to fine powder in an agate mortar.

Scanning electron microscopy (SEM) images were acquired on a Hitachi Regulus 8100 field emission scanning electron microscope operating at 10 kV. All samples were sputter-coated with platinum prior to imaging. Elemental mapping analysis was carried out using an Oxford Ultim Max 65 energy-dispersive X-ray (EDX) spectrometry system.

The total coke content was determined using an Analytik Jena Multi N/C 3100 total organic carbon (TOC) apparatus. Samples (~0.1 g) were combusted at 1000 °C for 5 min under an oxic atmospheric condition.

The GC-MS analysis of the CCl₄-soluble fraction of coke was performed on a 7890 A GC coupled to a 7000B triple quadrupole MS system (Agilent Technologies, Palo Alto, CA, USA). For GC analysis, the capillary column was DB-17MS (30 m × 0.25 mm × 0.25 µm). The oven temperature was held at 50 °C for 2 min, then ramped to 260 °C at 20 °C min⁻¹ and maintained isothermally for 5 min. Helium was used as the carrier gas at a constant flow rate of 1.0 mL/min. A 0.1 µL aliquot of the sample was injected in split mode (20:1) at 280 °C. For MS analysis, a full scan mode was used and the quality collection range was 28–650 Da. Identification of the compounds was carried out by comparing the retention times with the NIST database and quantification of soluble coke was performed using hexachloroethane (C₂Cl₆) as an internal standard.

The ¹³C solid-state MAS NMR spectra of the coked catalyst particles after separating soluble species were collected using a Bruker Avance III

400 MHz NMR spectrometer equipped with a 4 mm MAS probe head spinning at 10 kHz. Chemical shift values (δ) were reported in ppm and referenced to tetramethylsilane at 0 ppm. The curve-fitting analysis of the ^{13}C MAS NMR spectra was performed using OriginPro 2021 (OriginLab) software to determine the distributions of organic carbon functional groups in the insoluble coke [25,31].

XPS measurements of the as-prepared and spent catalysts were carried out on a VG Scientific ESCALAB 220i-XL spectrometer with a 300 W Al $\text{K}\alpha$ radiation source. Unless otherwise stated, all binding energies (BEs) were charge referenced to the adventitious carbon C 1 s peak at 284.8 eV. Quantitative analysis of XPS data including peak fitting was conducted using a Thermo Scientific Avantage software. Quantitative determination of the acidity of catalyst surfaces was carried out by temperature-programmed desorption of ammonia (NH₃-TPD), while the type and strength of the acid sites were probed with pyridine FTIR spectroscopy under various evacuation temperatures. Raman spectra of the as-prepared and spent catalyst samples were recorded at room temperature in the 200–2000 cm⁻¹ range on a Horiba Jobin-Yvon LabRAM HR800 UV system using a 632 nm He-Ne laser line with a power of 10 mW and a 50 \times objective lens (NA = 0.75, Olympus BX41 microscope). Prior to the measurements, the instrument was calibrated using the 520 cm⁻¹ Raman band signal of a silicon wafer.

3. Results and discussion

3.1. Characterizations of fresh and spent Mo-V/HMMT catalysts

The XRD patterns of MMT, HMMT, and Mo-V/HMMT catalysts are shown in Fig. 1a. For the pristine MMT, the diffraction peaks associated

with montmorillonite phase appear at $2\theta = 6.21^\circ$, 19.80° , 34.94° , 36.04° , and 61.91° , which can be assigned to the (001), (020), (110), (006), and (060) crystal planes, respectively [30,32]. Non-clay impurity phases, such as feldspars ($2\theta = 21.95^\circ$ and 28.62°) and calcite ($2\theta = 31.43^\circ$) were present in minor amounts in the MMT sample. The basal (001) spacing (d_{001}) value of MMT was calculated to be 1.42 nm according to the Scherrer equation, typical of Na-MMT accommodating two intercalated water layers [33]. After acid treatment with H₃PO₄ and loading Mo-V oxide particles, some changes in the (001) reflection were observed. The d_{001} reflection peak of HMMT becomes more prominent and shifts to a lower angle (5.51° 2θ), indicating an expansion of basal spacing from 1.42 nm for MMT to 1.60 nm for HMMT. The increase in basal spacing of ca. 0.18 nm could be reasonably ascribed to the cation exchange between hydrated Na⁺ ions and protons in MMT interlayers. Considering the difference between effective diameters of hydrated Na⁺ ions (0.45 nm) and protons (0.90 nm, [34]) and the observed interlayer expansion, it could be inferred that partial dehydration might occur during the drying process. This is in agreement with the previously reported result for acid treatment of MMT using low H₃PO₄ concentrations [32]. Moreover, acid treatment removes calcite impurity in MMT, as indicated by the disappearance of the diffraction peak at $2\theta = 31.43^\circ$ (black triangle). The use of different acid concentrations does not affect the interlayer spacing expansion in MMT (Figure S2a), but has a notable influence on the textural properties. As depicted in Figure S3a, the BET specific surface area (S_{BET}) of MMT ($33.1 \text{ m}^2 \text{ g}^{-1}$) increases considerably after H₃PO₄ treatment, reaching the highest value of $206.4 \text{ m}^2 \text{ g}^{-1}$ for 2HMMT, and followed by HMMT ($126.0 \text{ m}^2 \text{ g}^{-1}$) and 0.5HMMT ($95.3 \text{ m}^2 \text{ g}^{-1}$). Moreover, the BJH pore size distribution curves (Figure S3c) reveal that all HMMT samples exhibited higher mesopore volume with a main

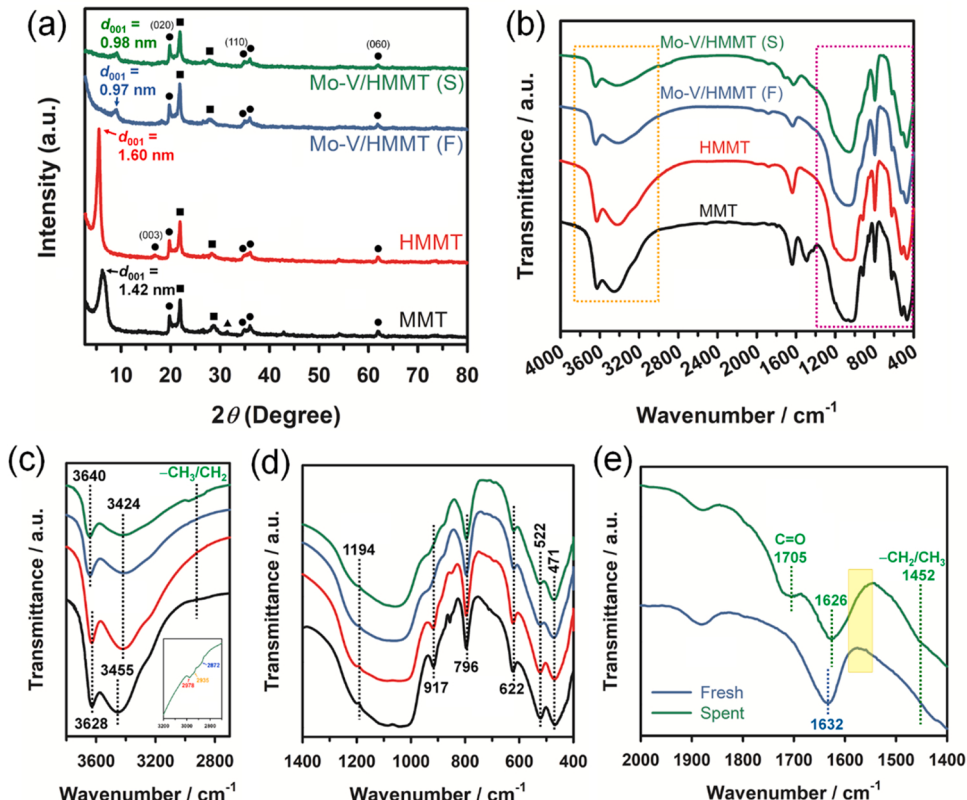


Fig. 1. (a) XRD patterns (● MMT; ■ feldspars; ▲ calcite) and (b) FTIR spectra of MMT, HMMT, and as-prepared (F) and spent (S) Mo-V/HMMT catalysts. Enlarged view of the wavenumber regions highlighted by dotted orange and magenta lines in (b): 3800–2700 cm⁻¹; the inset denotes the C–H vibrational region of the spent Mo-V/HMMT spectrum (green) for asymmetric CH₃ stretch, asymmetric CH₂ stretch, and symmetric CH₃ stretch at 2978, 2935, and 2872 cm⁻¹, respectively (c), 1400–400 cm⁻¹ (d), and 2000–1400 cm⁻¹ for the as-prepared and spent Mo-V/HMMT catalysts after 5 h of TOS (e). The light yellow rectangle in (e) denotes the wavenumber region of C=C stretching vibrations of unsaturated hydrocarbon compounds, such as polyaromatics, dienes, and olefins, which overlap with the OH bending band of water. Vertical dotted lines are drawn as a guide for the eye to observe the positions and some shifts of vibrational bands.

pore diameter of ~ 3.9 nm, being slightly larger than that of MMT (~ 3.6 nm).

The hydrated protons confined in MMT interlayers could serve as Brønsted acid sites for promoting dehydration of glycerol to acrolein, provided that they are accessible to the reactant molecules. The presence of the intense d_{001} reflection peak in HMMT materials implies that the interlayer structure was retained following acid treatment. On the contrary, the d_{001} peak is much weaker in Mo-V/HMMT and appears at a higher angle ($\sim 9.1^\circ$) than that of HMMT, suggesting a collapsed interlayer structure. This phenomenon can be ascribed to the removal of interlayer water during calcination and the calculated d_{001} spacing of 0.97 nm agrees well with literature values for dehydrated MMT [33,35]. The dehydrated state of the interlayer structure was also observed in Mo/HMMT and V/HMMT materials (Figure S4). The incorporation of Mo-V oxide particles leads to a slightly reduced S_{BET} of the support, from 126.0 to 119.4 m^2/g (Figure S3b), while the BJH mesopore size distribution remains similar to that of HMMT (Figure S3d). The density functional theory (DFT) PSD curves for slit-shaped pore model (Figure S5) reveal that the incremental pore volume in the meso-macropore range ($\sim 10\text{--}80$ nm) notably decreases for Mo/HMMT, V/HMMT, and Mo-V/HMMT materials, whereas the micropore volume peaked at 1.36 nm remains similar, suggesting that the metal oxide particles were mainly deposited in large mesopores or on the exterior surface of HMMT. This micropore size in Mo-V/HMMT is large enough to allow access of the glycerol molecules (0.515 nm) to the interior catalytic sites with virtually no diffusional resistance. Meanwhile, the reflection peaks associated with the crystalline Mo and V oxides (i.e., MoO_3 and V_2O_5) obtained by calcining the corresponding metal ammonium precursors at 500 $^\circ\text{C}$ (Figure S6) and their physical mixtures (Figure S7) prepared by mortar mixing of two components were absent in the XRD pattern of Mo-V/HMMT, implying either high dispersion of Mo-V species on the support surface and/or the loaded Mo-V-O particles have an amorphous or poorly crystalline structure. This may also indirectly infer that there exists a favorable interaction between Mo-V and the HMMT support. The spent Mo-V/HMMT after 5 h on stream showed a similar XRD pattern with the fresh one, indicating that the structure of the catalyst was maintained after reaction. In addition, the absence of the prominent (002) peak of graphite (JCPDS #75-1621) at 2θ of $\sim 26.2^\circ$ (Figure S8) confirmed the predominantly amorphous nature of the coke deposits formed [17].

Fig. 1b shows FTIR spectra of MMT, HMMT, and fresh/post-reaction Mo-V/HMMT materials. The wavenumbers of the vibrational bands and their respective assignments are given in Table S1. The bands at ~ 471 and $\sim 522 \text{ cm}^{-1}$ can be assigned to the bending vibrations of Si--O--Si and Al--O--Si bonds in MMT structure, respectively. The position and relative intensities of these two bands remain the same for all samples, indicating that the structural integrity of MMT was retained after acid treatment, Mo-V particle deposition, and catalytic glycerol oxydehydration, consistent with the XRD results in Fig. 1. The weak band at 917 cm^{-1} and the broad intense one centered around 1068 cm^{-1} correspond to the Al--Al--OH bending and tetrahedral Si--O stretching vibrations of MMT, respectively. Compared to MMT, the intensity of the Al--Al--OH band in HMMT is weaker, which could be attributed to the acidic leaching of octahedral Al^{3+} ions. The extent of Al leaching is more pronounced for 2HMMT (Figure S2b), as evidenced by the stronger decrease in the Al--Al--OH , Al--O--Si , and Si--O--Si band intensities. Such the removal of aluminum atoms in the octahedral sheets generates coordinatively unsaturated Al^{3+} centers that can act as the active Lewis acid sites [30,36]. The carbonate (CO_3^{2-}) stretching peak of calcite present in MMT at $\sim 1429 \text{ cm}^{-1}$ is absent in HMMT, indicating the removal of this trace mineral impurity during acid activation treatment.

The OH bending and stretching modes of the interlayer water molecules appear at 1626 and 3455 cm^{-1} , respectively. In the case of the latter, an obvious shift of the band to lower wavenumber was observed for HMMT (red line in Fig. 1c), likely due to the change in the interlayer organization of water during exchange of H^+ for Na^+ . The OH stretching

band at $\sim 3630 \text{ cm}^{-1}$ correlates with the vibration of the hydroxyl groups coordinated to Al octahedra [37]. For the as-prepared and spent Mo-V/HMMT materials (Fig. 1c, blue and green lines, respectively), this band blue-shifts by $\sim 10 \text{ cm}^{-1}$ to higher wavenumbers, probably due to modification of the octahedral Al framework upon the incorporation of Mo-V species. Similar results were observed in the FTIR spectra of Mo/HMMT and V/HMMT (Figure S9). In addition, the Al--Al--OH peak at $\sim 917 \text{ cm}^{-1}$ in these spectra is attenuated and appears as an inflection. On the basis of these spectral bands and previous study of Kwak et al. [36], it can be inferred that the coordinatively unsaturated Al^{3+} cations at broken octahedral edges may serve as the anchoring sites for Mo-V species. However, no noticeable vibrational features associated with Mo-V oxides, such as terminal Mo=O and bridging Mo--O--Mo bands of bulk MoO_3 at ~ 1000 and $\sim 820 \text{ cm}^{-1}$, respectively [38,39]; V=O stretching of vanadyl groups at $\sim 1030\text{--}1050 \text{ cm}^{-1}$ and Al--O--V stretch at $\sim 930\text{--}955 \text{ cm}^{-1}$ [40]; and V--O--Mo bending at $\sim 600 \text{ cm}^{-1}$ [41] were observed in the Mo-V/HMMT spectrum. A probable reason for this is the aforementioned vibrational modes have relatively weak intensities and are thus covered by vibrations of HMMT. This may also imply that the Mo-V-O particles deposited on the HMMT surface are well dispersed and present at low loading amount, showing good agreement with XRD analysis.

The intensities of the OH stretching and bending bands of interlayer confined water at 3435 and 1626 cm^{-1} for fresh and spent Mo-V/HMMT materials decreased compared with those of HMMT, which correlate well with the dehydrated layers of MMT after calcination at 500 $^\circ\text{C}$. Meanwhile, the FTIR spectrum for spent Mo-V/HMMT revealed molecular vibrations of hydrocarbon species at 3000–2850, ~ 1705 , and $\sim 1450 \text{ cm}^{-1}$, which are readily assignable to the CH_3/CH_2 asymmetric and symmetric stretches (see Fig. 1c inset), C=O stretching, and CH_3/CH_2 bending, respectively. Moreover, a closer analysis of the 1400–2000 cm^{-1} region of the spent catalyst spectrum reveals a broad tail extending to $\sim 1550 \text{ cm}^{-1}$ on the low wavenumber side of the OH bending band (yellow highlighted region in Fig. 1e). This region corresponds to the C=C stretches in unsaturated hydrocarbon compounds, such as olefins, dienes, and polyaromatics [26,42,43]. Compared to the fresh catalyst, the OH bending band of water for spent Mo-V/HMMT is broader and red-shifts from 1632 to 1626 cm^{-1} , likely due to the presence of superimposed C=C vibrations. The presence of these organic functional groups corroborates the formation of carbon deposits on the catalyst during glycerol oxydehydration, whose chemical structure consists of linear alkanes, aromatics, and carbonyl compounds (i.e., aldehydes, ketones, or carboxylic acids) [38]. In addition, the polyaromatic coke structures appear to be highly alkylated [42,43], as evidenced by the absence of C-H stretching mode at 3000–3100 cm^{-1} . More in-depth discussion of the nature of coke deposited on the catalyst is presented in later sections by Raman spectroscopy, GC-MS, ^{13}C solid-state MAS NMR, and XPS analyses.

The valence states of Mo and V in the as-prepared Mo/HMMT, V/HMMT, and Mo-V/HMMT catalysts were examined by XPS (Fig. 2). As can be seen in Fig. 2a, the Mo 3d XPS spectrum of Mo/HMMT (bottom) exhibits four peaks associated with the Mo $3d_{5/2}$ and Mo $3d_{3/2}$ spin-orbit components of high valent Mo(VI)-oxo species. Specifically, the Mo $3d_{5/2}$ -Mo $3d_{3/2}$ doublet at 232.5 and 235.8 eV with an energy separation (ΔE) of 3.3 eV can be assigned to the three-dimensional polymeric Mo (VI)-oxo species exhibiting weak electronic interactions with the support, while another doublet at 234.8 and 238.0 eV ($\Delta E = 3.2 \text{ eV}$) corresponds to the Mo(VI)-oxo species that strongly interact with the support. This latter Mo(VI) oxo species has been observed as well for highly dispersed molybdena supported on alumina and silica [44], both of which are the principal chemical constituents of MMT. Moreover, the proportion of strongly interacting Mo(VI)-oxo surface species, calculated as the ratio of its peak area to the total Mo 3d area, was also found to increase with a higher ratio of Mo/(Mo+V). Meanwhile, the high-resolution V 2p_{3/2} XPS spectrum of V/HMMT (Fig. 2b bottom) can be well deconvoluted into two peaks centered at 516.7 and 518.0 eV,

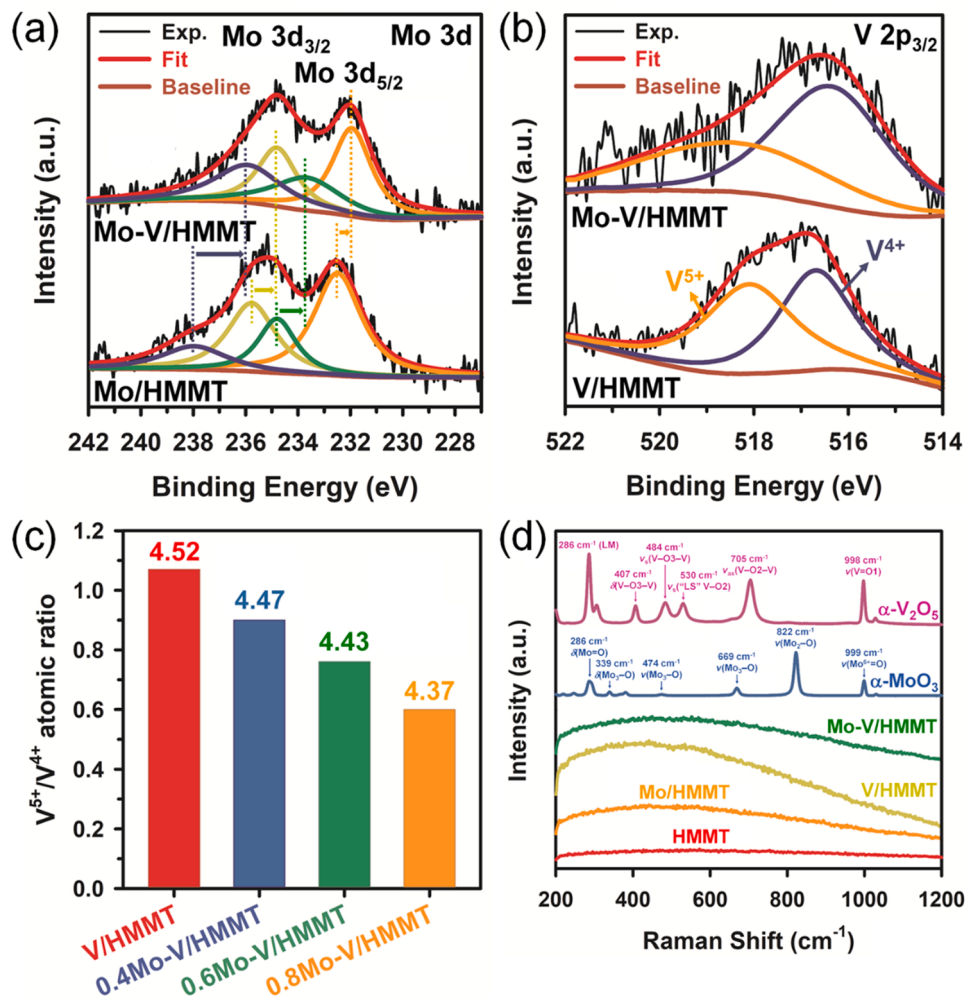


Fig. 2. Surface chemical analysis of Mo/HMMT, V/HMMT, and Mo-V/HMMT catalysts. High-resolution XPS spectra of (a) Mo 3d and (b) V 2p_{3/2}. (c) Atomic ratios of V⁵⁺/V⁴⁺ determined from the proportion of the integrated peak areas of each component. Numbers on top of each bar represent the average valence state of V in the corresponding as-prepared catalysts. (d) Raman spectra at 632 nm excitation of HMMT, Mo/HMMT, V/HMMT, and Mo-V/HMMT. The Raman band of a silicon wafer with maxima at 520 cm⁻¹ was used for system calibration. For HMMT and the supported catalyst samples, some very weak bands were barely observable in the spectra, due to the strong fluorescence level from MMT (see Fig. S10a-d). The notations of LM and LS for Raman bands of α -V₂O₅ at 286 and 530 cm⁻¹ denote ladder mode and ladder steps, respectively.

corresponding to the vanadium in the + 4 and + 5 oxidation states, respectively. The BEs of the V⁴⁺ and V⁵⁺ 2p_{3/2} peaks are in good agreement with values reported in the literature [45–47]. The surface V⁴⁺ species, which is readily formed upon calcination of supported vanadia phase in air, accounts for about 48% of the total amount of V, resulting in an average V valence state of 4.52 for V/HMMT (Fig. 2c). With regard to Mo-V/HMMT catalyst (Mo/(Mo+V) ratio = 0.8), the Mo 3d_{5/2}-Mo 3d_{3/2} doublets showed an obvious shift to lower BE relative to those of Mo/HMMT (Fig. 2a and b, upper panel). In addition, the contribution of surface V⁵⁺ species on the Mo-V/HMMT catalysts decreases with the increase in Mo/(Mo+V) ratio, leading to a decrease in the average valence state of V from 4.47 to 4.37 (Fig. 2c). This result indicates that there is a strong electronic interaction between Mo and V in the Mo-V/HMMT catalysts through electron transfer from V to Mo. Raman spectra at 632 nm laser excitation for HMMT, Mo/HMMT, V/HMMT, and Mo-V/HMMT materials are shown in Fig. 2d. Reference spectra for pure orthorhombic MoO₃ and V₂O₅ crystal phases (see XRD patterns in Figure S6a,b) were also included for the sake of examining the dispersion state of metal oxo species on the HMMT surface, in which the obtained Raman features in the 200–1200 cm⁻¹ region show excellent agreement with the literature [39,45,48]. As can be seen in Fig. 2d, Raman spectra of the as-prepared catalyst samples in the 200–1200 cm⁻¹

region exhibit a featureless broad hump, which could be attributed to the presence of a strong fluorescence signal from MMT (Figure S10a-d). Similar observations have been previously reported by Ritz et al. [49] in Raman analysis of various well-defined MMT minerals using 532 and 780 nm laser excitations. Nevertheless, the Raman bands associated with crystalline orthorhombic MoO₃ and V₂O₅ were absent in the spectra of all the as-prepared materials, suggesting well-dispersed metal oxide species on the support.

The morphology of the fresh (as-prepared) and coked Mo-V/HMMT catalysts was examined by SEM. As depicted in Fig. 3a, the HMMT particles exhibited a rougher surface with few broken edge structures compared to the pristine MMT, which leads to an increased specific surface area and porosity of the support material (see Figure S3). After impregnation of Mo and V metal precursors and subsequent air calcination at 500 °C, the lamellar structure of MMT is still apparent (Fig. 3b), in agreement with interpretation of XRD and FTIR results. SEM-EDX elemental mapping analysis revealed a uniform distribution of major constituent elements (i.e., Si, Al, and O) of MMT, as well as Mo and V in the Mo-V/HMMT particles (Figure S11). This result may imply that the co-impregnation–calcination conditions employed in this work yielded well-dispersed Mo-V-O species on the HMMT support, consistent with results obtained from XRD and Raman characterization. The

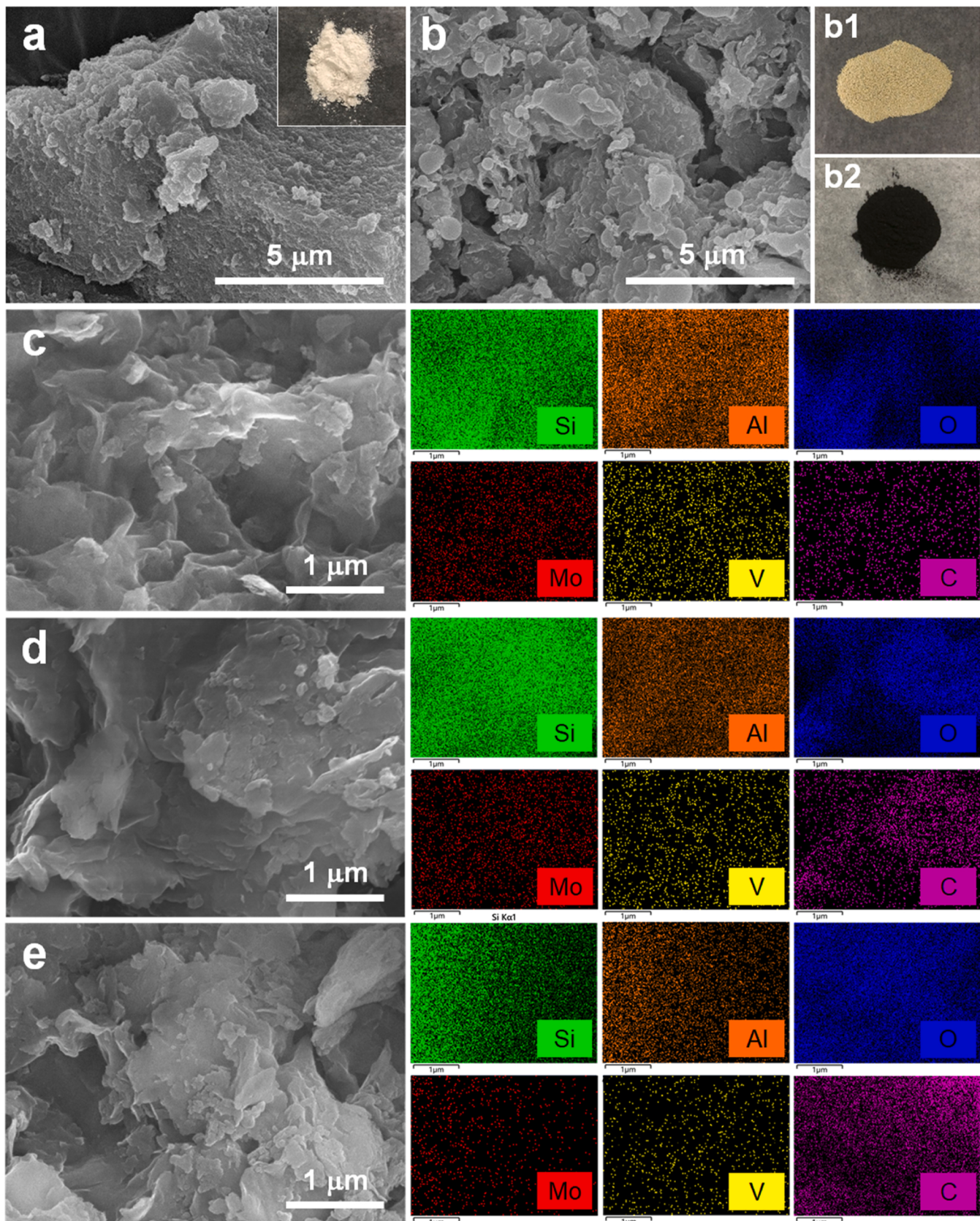


Fig. 3. . SEM images of (a) HMMT (Inset: photograph of the powder sample) and (b) fresh and (c-e) spent Mo-V/HMMT catalysts (nominal Mo/(Mo+V) mole ratio = 0.8) collected at TOS of (c) 1 h, (d) 3 h, and (e) 5 h, along with the corresponding EDX elemental mapping. Top right image shows the photographs of Mo-V/HMMT catalysts (b1) before and (b2) after being used for 5 h of gas-phase glycerol oxydehydration reaction. For the spent (coked) catalysts, the reaction conditions used are as follows: $T = 320$ °C, carrier gas = air at 21 mL/min, reactant feed = 20 wt% aqueous glycerol solution (0.1 mL/min).

homogeneous distribution of Mo and V elements throughout the Mo/HMMT and V/HMMT catalyst particles, respectively was also evidenced by their corresponding SEM-EDX elemental maps (Figure S12). Fig. 3c-e shows the typical SEM images of the spent Mo-V/HMMT catalysts after 1, 3, and 5 h on stream of gas-phase glycerol oxydehydration reaction at 320 °C, respectively. The results showed that the spent catalyst particles had visibly smoother surface topography with fewer wrinkles than that of the as-prepared ones, which could be attributed to the coke coverage on the catalyst surface. The formation of carbon deposits on the spent Mo-V/HMMT catalyst surface was also confirmed by the black appearance of the sample (Figure 3b2), as well as by the elemental mapping of carbon. The coke formation over the catalyst was found to significantly affect the textural properties. As can be seen from Figure S13a, the S_{BET} and V_{T} values of Mo-V/HMMT catalyst drastically decreased from 119.4 to 19.6 m^2/g and from 0.23 to 0.17 cm^3/g after 5 h TOS. In addition, the DFT pore size distributions showed that both micropores and small mesopores ($\sim 3 \text{ nm}$) were completely absent in the spent catalyst, whereas larger mesopores ($>6 \text{ nm}$) and macropores ($>50 \text{ nm}$) remained relatively unaffected (Figure S13b). This result implies that the formation of deactivating coke deposits is detrimental for micropores and

mesopores smaller than about 5 nm in diameter, which may explain a considerably greater decrease ($\sim 84\%$) in surface area of the catalyst relative to the pore volume ($\sim 26\%$). The blocked micro- and small mesopores could significantly retard the diffusion of reactant and product molecules into and out of the catalyst [50], thus affecting catalyst activity and TOS stability (*vide infra*). Meanwhile, the coke deposition on large pore surfaces had a lesser effect on mass transport of reactant and product species, and consequently a low deactivating effect.

3.2. Catalytic performances of Mo/HMMT, V/HMMT, and Mo-V/HMMT

The gas-phase catalytic glycerol oxydehydration over Mo-V/HMMT (nominal Mo/(Mo+V) mole ratio = 0.8) was performed at 320 °C and atmospheric pressure. As can be seen from Fig. 4a, a high glycerol conversion of 91.4% and acrolein selectivity of $\sim 52\%$ was achieved using this catalyst at 1 h TOS. By comparison, Mo/HMMT exhibited a significantly lower catalytic activity ($\sim 57\%$ conversion), whereas V/HMMT demonstrated similar performance to Mo-V/HMMT with $\sim 90\%$

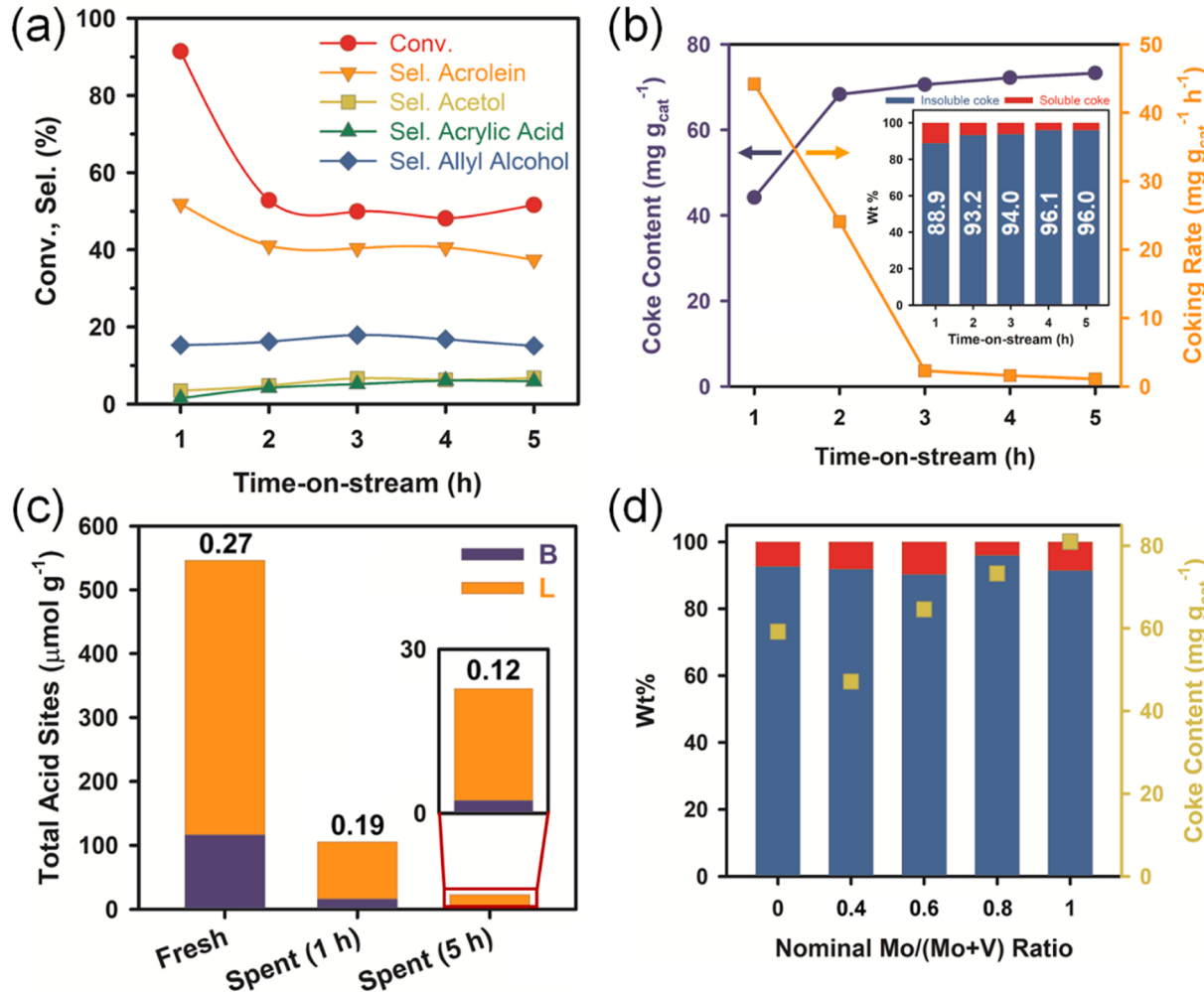


Fig. 4. . Catalytic performance of Mo-V/HMMT in the gas-phase oxydehydration of glycerol. (a) Conversion and selectivity plots of different products with TOS. (b) Coke content of the spent catalysts determined by TOC analysis and the coking rate as a function of TOS. The inset shows the proportions of soluble (red bars) and insoluble cokes (blue bars) with TOS. The numbers in white correspond to the weight percentage of insoluble coke. Soluble coke was calculated by subtracting the insoluble coke from the total coke amount quantified by TOC analysis. (c) Distribution of Brønsted (B) and Lewis (L) acid sites in fresh and spent Mo-V/HMMT catalysts (Mo/(Mo+V) ratio = 0.8) at TOS of 1 and 5 h, as determined by FTIR spectroscopy of pyridine adsorption. Numbers on top of each bar represent the ratio of B/L acid sites. (d) Coke content (yellow squares) in the spent Mo-V/HMMT catalysts with varying Mo/(Mo+V) mole ratios after a TOS of 5 h. The red and blue bars denote soluble and insoluble coke fractions, respectively. Reaction conditions: mass of catalyst = 0.5 g, $T = 320 \text{ }^{\circ}\text{C}$, carrier gas = air at 21 mL/min, and reactant feed = 20 wt% aqueous glycerol solution (0.1 mL/min).

conversion (Figure S14a). In addition, both the Mo/HMMT and V/HMMT catalysts were found to deactivate faster than Mo-V/HMMT within the 5 h catalytic tests (Figure S14b), which may suggest the synergistic interplay between Mo and V elements in enhancing the coking resistance of the catalyst. In particular, the Mo-V/HMMT catalyst with a nominal Mo/(Mo+V) mole ratio of 0.4 showed the lowest deactivation rate (~29%); however, it also gave the lowest initial catalytic activity (~59% conversion) compared with two other catalysts. The reason for this could be attributed to the concentration of acidic sites on the catalyst surface, which is determined by FTIR spectroscopy of pyridine adsorption. As shown in Figure S15, the total amount of acid sites (both Brønsted and Lewis) on Mo-V/HMMT (Mo/(Mo+V) mole ratio = 0.4) was remarkably lower (234.5 $\mu\text{mol g}^{-1}$) than those on HMMT (882.1 $\mu\text{mol g}^{-1}$) and Mo-V/HMMT catalyst with a Mo/(Mo+V) ratio of 0.8 (545.9 $\mu\text{mol g}^{-1}$), which explains both the low catalytic activity and reduced coking level of this catalyst. With an increase in the Mo content, the initial conversion of glycerol was significantly enhanced, reaching 91.4% at a nominal Mo/(Mo+V) mole ratio of 0.8, while at the same time inducing faster deactivation of the catalysts with TOS. We further examined the strength of the acid sites in Mo-V/HMMT catalysts by looking at the acid site fractions that were preserved upon stepwise pyridine desorption under vacuum at elevated temperatures (200–350 °C). While the support material (HMMT) itself possesses strong acidity, particularly Brønsted type with a B/L ratio of 3.1 upon evacuation at 350 °C (Figure S16), the Mo-V/HMMT catalysts contain Brønsted and Lewis acid sites of medium strength (Figure S17), as confirmed by the gradual decrease of band intensity of the adsorbed pyridine at 1445, 1491, 1543, 1599, and 1633 cm^{-1} with increasing desorption temperatures (see Table S2 for band assignments). The band at 1581 cm^{-1} could be assigned to pyridine molecules bonded to the surface hydroxyl groups, which shifted slightly to lower wavenumber (~1577 cm^{-1}) and almost completely vanished after evacuation at 200 °C, thus indicating its weak acidic strength. This result suggests that the incorporation of Mo-V into HMMT framework not only reduces the amount of acid sites, but also decreases the relative strength of the Brønsted and Lewis acid sites, eventually leading to the lower coking rate of the catalysts. The B/L ratio in the Mo-V/HMMT (0.26–0.27) is much lower than that in HMMT (0.88) and it increases upon desorption at higher temperatures (Figures S15b and S17c,d). Another important point that deserves mention here is that, although Mo-V/HMMT catalysts with Mo/(Mo+V) ratios of 0.4 and 0.8 have similar B/L values, the latter exhibits new strong Brønsted acid sites at 1651 and 1682 cm^{-1} (Figure S18b). These acid sites (present in minor amounts) likely arise from local interactions between Mo-V species and HMMT, and may contribute to higher catalytic activity of this catalyst compared to one with a Mo/(Mo+V) ratio of 0.4. A new infrared band at 1654 cm^{-1} assigned to pyridine chemisorbed on Brønsted acid sites was also observed in the Mo-V/HMMT catalyst with a Mo/(Mo+V) ratio of 0.4 (Figure S17) but this band vanishes upon desorption treatment at temperatures above 200 °C, which verifies the weaker strength of this acid site.

The acrolein space time yield of 724.82 $\text{g}\cdot\text{kg}_{\text{catalyst}}^{-1}\cdot\text{h}^{-1}$ for Mo-V/HMMT with a Mo/(Mo+V) ratio of 0.8 is notably higher than those of other reported catalysts, such as vanadium pyrophosphate [47], acid-treated V_2O_5 [51], and supported Mo- or V-containing heteropolyacids [52,53] (Figure S19), demonstrating the potential for acrolein production from glycerol. Apart from acrolein, allyl alcohol was detected in the condensed liquid product on this catalyst with an appreciable selectivity of about 15%. The formation of this compound may arise either from selective hydrogenation of the $\text{C}=\text{O}$ bond of acrolein through a hydrogen transfer reaction with glycerol and OH-containing intermediates as the hydrogen donor [54] or from a radical-promoted dehydroxylation reaction of glycerol as proposed by Smith et al. [55]. Other subproducts formed in low selectivities (<10%) include 1-hydroxyacetone (acetol), acetaldehyde, acetone, propionic acid, and acrylic acid; the latter compound is the partially oxidized product of acrolein.

The selectivities of these oxygenates with TOS can be found in Table S3. In addition, the total selectivities of C_2 and C_3 oxygenates after 5 h TOS were found to be quite similar for the V/HMMT and Mo-V/HMMT catalysts (~60–67%), but it is considerably lower for the Mo/HMMT (36.2%). The low propensity for acetol formation (6–7% selectivity) in the present catalytic system suggests that the dehydration of glycerol at the terminal OH group does not favorably occur over Mo-V/HMMT. In contrast, acrolein (another dehydration product of glycerol) was observed as the main reaction product with ~52% selectivity, which implies that the glycerol molecules preferentially dehydrate through protonation of the central hydroxyl group over Brønsted acid sites in the catalyst. Acrylic acid, an industrially important oxygenate, was obtained in the reaction using Mo/HMMT, V/HMMT, and Mo-V/HMMT as catalysts, while this product was not formed in catalytic tests with HMMT (Figures S14a and S20a). This confirms that the addition of Mo-V not only facilitates partial oxidation of acrolein to acrylic acid through a Mars–van Krevelen redox mechanism but also can inhibit coke formation on the surface of the catalyst particles (filled bars in Figure S20b). In accordance with this result, the extent of deactivation is notably lower for Mo-V/HMMT compared to their corresponding HMMT supports under the same reaction conditions. Although Mo-V/HMMT catalysts showed better TOS stability and good catalytic activity for acrolein production, the yield of higher-value acrylic acid was very low (2–3%). This could be attributed to the low loading and sparse distribution of Mo-V species on the support, as has been demonstrated by XRD, SEM, and Raman analyses. Propionic acid ($\text{C}_3\text{H}_6\text{O}_2$) is another high-value oxygenate, which could be formed either through isomerization of acetol [17,18] or partial oxidation of propanal.

After 1 h TOS, the glycerol conversion of the Mo-V/HMMT dropped rapidly from 91.4 to 51.8%, after which it remained fairly constant at around 50% over the remainder of the reaction. Similarly, the acrolein selectivity showed a modest decrease (from 52 to 41%) at 2 h TOS, before stabilizing at 38–40%. These results demonstrate that significant deactivation of the catalyst occurred within the first two hours of reaction, due to blocking of active sites in micro- and small mesopores by carbon deposits. The formation of deactivating carbon deposits during this initial period may block parts of the catalytic sites responsible for the production of unknown products and/or coking that leads to stabilization of the catalyst surface. The conversion-selectivity plot versus TOS (Fig. 4a) further supported this argument by showing that both the glycerol conversion and acrolein selectivity of the catalyst remain relatively stable after 2 h TOS, which may also imply that the Brønsted acid sites in Mo-V/HMMT are not completely blocked by the coke and thus the catalyst still retains a considerable portion of its initial activity. The relatively stable selectivity to acrolein after 2 h TOS suggests that the formation of this C_3 oxygenate is not or minimally affected by diffusion limitations, due to the presence of mesopores in the catalyst. Such a relationship between pore size and the acrolein selectivity was also observed in other studies [17,50]. It should be noted, however, that coke formation indeed takes place in the early stages of the reaction, that is, in parallel with double dehydration of glycerol to acrolein, as corroborated by Raman and TOC analyses of the spent catalyst at 1 h TOS (Fig. 4b and S21). Moreover, while both the conversion and acrolein selectivity decreased over the first 2 h, the acetol and acrylic acid selectivities slightly increased from 3.5 to 4.8% and from 1.5 to 4.2%, respectively and they continue to slightly increase for 5 h on stream. Meanwhile, the allyl alcohol selectivity remained relatively unchanged at ~15–17% throughout the 5 h TOS test. These results therefore suggest that blocking of active sites, particularly those with strong Brønsted acidity, by carbon deposits during the early reaction stages could promote the propensity of glycerol molecules for Lewis acid sites, leading to increased formation of acetol and its secondary products, such as acetone and propionic acid (Table S3). Despite being the main descriptor for acrolein formation, strong Brønsted acid sites are also responsible for side reactions leading to catalyst coking, as shown in other studies [23]. The promotional effect of such coke-site blocking on

the product selectivity was also observed by Possato et al. [16] and Hita et al. [56].

TOC analysis was employed to quantify the amount of carbon deposited on the catalyst surface during the glycerol oxydehydration reaction. Combined with the extraction experiments described in Section 2.4, quantitative information regarding the TOS evolution of soluble and insoluble coke species can be obtained. Before discussing the results, the structural information on coke deposits, including the carbon functional groups was gained from Raman spectroscopy, as shown in Figure S21. Compared with the typical Raman spectrum of bulk graphite comprising well-separated D and G bands at around 1360 and 1580 cm⁻¹, respectively (data not shown), the Raman spectra of the spent Mo-V/HMMT catalysts in the 1200–1800 cm⁻¹ region feature a broader and merged band with maxima at around 1420 and 1630 cm⁻¹. Indeed, these Raman bands are considerably blue-shifted compared to the D and G bands of graphite, suggesting that the deposited carbon on the spent catalyst has an amorphous structure and shows good agreement with the XRD results. The formed coke can also be considered as low sp³ amorphous carbon [57]. To gain further insights into the organic carbon functional groups in amorphous coke, the Raman spectra were deconvoluted into their respective components using Gaussian function. As can be seen in Figure S21a-c, the deconvoluted spectra consist of five bands centered at around 1290, 1420, 1540, 1630, and 1630 cm⁻¹, which can be assigned to the vibrational frequencies of the C-C stretching in aliphatic chains, CH₂ and CH₃ asymmetric deformation (δ) modes, C=C and C-C stretching of benzenoid aromatic rings, and symmetrical C=O stretching, respectively [58,59]. The relative contents (%) of these carbon functional groups were estimated based on the ratio of the individual peak area to the total peak area, as presented in Figure S21d. Notably, the coke molecules deposited on the catalyst surface are predominantly aromatic and the increase in aromatic carbon content at longer TOS may suggest the formation of more condensed polycyclic aromatic molecules. Further details on the possible chemical structure of the deposited coke on the Mo-V/HMMT catalyst will be discussed later. An evident decrease in the relative content of aliphatic carbon with TOS was also observed.

The changes in the soluble and insoluble fractions of coke as a function of TOS are depicted in Fig. 4b. It can be seen that a relatively small amount of coke (4.4 wt%) was formed on the catalyst surface during the first hour on stream and it increased sharply to 6.8 wt% within 2 h TOS. This result correlates well with the trends observed for the glycerol conversion and acrolein selectivity at TOS < 2 h, as has been described earlier. After 2–5 h TOS, the coke formation on Mo-V/HMMT catalyst proceeded much slower with an average coking rate of 1.67 mg·g_{catalyst}⁻¹·h⁻¹, as compared to 34.15 mg·g_{catalyst}⁻¹·h⁻¹ during the first 2 h (orange line in Fig. 4b). This observation agrees well with other published reports [60,61]. The decreased rate of coking at longer TOS can be attributed to the reduction in the number of acidic active sites on the catalysts, as confirmed by pyridine adsorption analysis. Fig. 4c shows that the total amount of acid sites in Mo-V/HMMT catalyst decreased drastically within 1 h of reaction, implying fast coke formation at the early stages of the process. After 5 h on stream, the number of acidic sites on the catalyst was further decreased but to a much lower extent than that observed in the early stages, which is in line with the slowing rate of coking. Moreover, the observed decrease in B/L ratio, as well as the proportion of Brønsted acid sites to total amount of acid sites with TOS may suggest that the Brønsted acid sites are preferentially deactivated by coke than the Lewis ones. With respect to the soluble and insoluble coke components, the latter constitutes a majority of the bulk coke deposited on the catalyst surface, even at the early stage of TOS (blue bars in Fig. 4b). The amounts of coke formed in Mo-V/HMMT catalysts with varying nominal Mo/(Mo+V) mole ratios (the values of 0 and 1 correspond to the V/HMMT and Mo/HMMT, respectively) after 5 h reaction were examined (yellow squares in Fig. 4d), showing different degrees of coking. As can be seen, the V/HMMT catalyst exhibited greater resistance to coking than the Mo/HMMT during the

reaction, as evidenced by considerably lower amount of coke produced (i.e., 59.2 mg g⁻¹ for V/HMMT versus 81.0 mg g⁻¹ for Mo/HMMT). For the Mo-V/HMMT catalysts, the results showed that there is a relationship between the Mo/(Mo+V) ratio and coking level, in which increasing the proportion of Mo (or higher Mo/(Mo+V) ratio) leads to more coke formation. The coking level of Mo-V/HMMT materials was positively correlated with the total amount of acid sites in the catalyst as described earlier.

Furthermore, the effect of HMMT support materials on the coking behavior of Mo-V/HMMT catalyst was investigated (filled bars in Figure S20b). More cokes are formed during the catalytic gas-phase oxydehydration of glycerol over Mo-V/2HMMT (7.8 wt%) in comparison with the Mo-V catalysts supported on 0.5HMMT (5.2 wt%) and HMMT (7.3 wt%). Because all of the as-prepared HMMT supports possess similar pore structures according to the N₂ sorption analysis (Figure S3d), the above results can be correlated to the amount of acid sites on the catalyst surface [62]. Indeed, the NH₃ TPD analysis (Figure S22) showed that the amount of acid sites was the highest for Mo-V/2HMMT (1.76 mmol g⁻¹ compared to 1.67 mmol g⁻¹ for Mo-V/0.5HMMT and 1.70 mmol g⁻¹ for Mo-V/HMMT), leading to pronounced coking on this catalyst. Compared with the pyridine adsorption method, the NH₃ TPD probes higher number of acid sites in Mo-V/HMMT, which can be ascribed to the higher accessibility of NH₃ to the acid sites, including those in smaller pores, than pyridine [63]. The NH₃ desorption peaks appearing at low (<200 °C) and high temperatures (>650 °C) could be attributed to weak and very strong acid sites [50], respectively. Specifically, these weak and very strong acid sites correspond to the physisorbed NH₃ and the Si-O(H)-Al groups of HMMT, respectively, which agreed well with the previous report [64]. For Mo-V/2HMMT catalyst, the high-temperature desorption peak maxima was observed at around 697 °C, notably higher than those of Mo-V/0.5HMMT (655 °C) and Mo-V/HMMT (675 °C). Moreover, a weak hump was also observed at around 438 °C, which corresponds to desorption of NH₃ from medium/strong Lewis acid sites associated with Mo-V coordinated to unsaturated Al³⁺ sites. The coke formation on the catalyst surface is also thought to be influenced by the glycerol feed concentration. As depicted in Figure S23, higher glycerol feed concentrations correlated with increased coke formation and consequently led to a greater catalyst deactivation. The fraction of insoluble coke increases from 88.9 to 96.0% with TOS, whereas the soluble one decreases gradually from 11.1 to 4.0% (Fig. 4b), suggesting that part of the soluble coke was transformed to insoluble one. This observation is in agreement with the trend observed in coke formation during the methanol-to-olefins process [25,65], indicating that the growth of insoluble coke on Mo-V/HMMT catalysts during gas-phase glycerol oxydehydration may proceed via extension or condensation of soluble coke.

The coked Mo-V/HMMT catalysts can be easily regenerated for reuse by a mild calcination process. To determine the optimal regeneration temperature, calcination treatments of the spent catalyst were conducted in the temperature range of 300–500 °C for 4 h and the regenerated catalyst materials were probed by FTIR spectroscopy to examine any remaining carbon deposits. As depicted in Figure S24, the ATR-FTIR spectrum of the calcined spent catalyst at 300 °C showed vibrational bands associated with HMMT and an additional peak at 1428 cm⁻¹ that corresponds to the aromatic C-C ring stretching vibration. Clearly, this latter band attributable to coke was absent in the Mo-V/HMMT catalysts regenerated at 400 and 500 °C. The incomplete removal of coke deposits on the regenerated catalyst at 300 °C is also visually evidenced by a dark gray color of the sample. Meanwhile, the spent catalysts treated at 400 and 500 °C displayed a light gray and light yellow color, respectively, with the latter being similar to that of the as-prepared one, and their corresponding ATR-FTIR spectra showed only vibrational signatures of HMMT, that is, Al-OH stretching (~3649 cm⁻¹), Si-O stretching (~1048 cm⁻¹) Al-O/Si-O out-of-plane deformation (~620 cm⁻¹), and Si-O-Si bending (~480 cm⁻¹). The regenerated Mo-V/

HMMT catalysts at 400 and 500 °C were further tested for gas-phase glycerol oxydehydration under the same reaction conditions as the fresh coke-free sample (Figure S25). A 38.1% selectivity to acrolein at 68.8% glycerol conversion was achieved over the regenerated catalyst at 500 °C after a TOS of 1 h, yielding an acrolein productivity (STY) of 352.7 g·kg⁻¹_{catalyst}·h⁻¹. These conversion and selectivity levels are slightly lower than that of the fresh catalyst (71.6% conversion and 41.8% acrolein selectivity). The acrolein STY still reached 344.2 g·kg⁻¹_{catalyst}·h⁻¹ upon reusing the same catalyst material twice, which is well comparable to that of the as-prepared state, and indicated that the Mo-V/HMMT catalyst possesses good reusability. For the spent Mo-V/HMMT catalyst regenerated at 400 °C, its catalytic activity in terms of glycerol conversion and acrolein selectivity was notably lower than that of the regenerated catalyst at 500 °C. This implies that an appreciable portion of coke still remains in the catalyst after the thermal treatment at 400 °C and that these carbon deposits, probably resides in the internal pore spaces, may obstruct access to the active sites. Although the nature of retained coke species was not investigated further, it can be reasonably inferred based on the oxygen temperature-programmed oxidation from a previous study [66] that the carbon deposits are amorphous, which typically require a high temperature at or near 500 °C to remove.

3.3. Chemical composition of coke as a function of TOS

3.3.1. Soluble coke

Fig. 5 shows the GC-MS chromatograms of the CCl₄-soluble coke components of spent Mo-V/HMMT catalysts collected at 1, 3, and 5 h TOS. Obviously, the chromatograms of organic extracts reveal distinct differences, indicating that the soluble coke composition changes with TOS. The detailed composition and relative abundances of organic compounds in soluble coke extracts are presented in Table 1. As can be seen, the soluble coke molecules are composed of both mononuclear aromatic derivatives (peaks A1, A2, and A3) and aliphatic hydrocarbons (peaks B1-B7). Note that the C₂Cl₆ peak in the chromatograms corresponds to the internal standard for quantification of coke species dissolved in CCl₄.

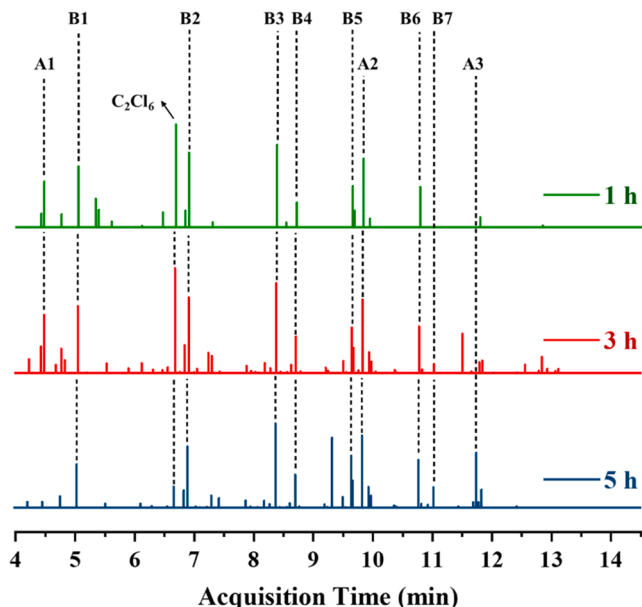


Fig. 5. GC-MS chromatograms of CCl₄-soluble coke components on spent Mo-V/HMMT catalysts after 1, 3, and 5 h on stream. For simplicity, only the major peaks are labeled in the chromatograms. The detailed information about labeled peaks and their relative abundances can be found in Table 1. The C₂Cl₆ peak at a retention time of 6.5 min corresponds to the internal standard for quantification.

The major mononuclear aromatic derivatives present in soluble coke at TOS of 1 and 3 h were xylenes (A1) and 2,4-di-tert-butylphenol (A2). Xylenes are most likely formed from the acid-catalyzed aldol condensation of short-chain oxygenates, such as acetol, acetone, and acetaldehyde, followed by cyclization and aromatization reactions [19,67,68]. Luo and Falconer [69] have also reported that acetone and acetaldehyde both readily form trimeric condensation products over Brønsted acid sites, namely 1,3,5-trimethylbenzene (mesitylene) and hexan-2,4-diene-al, respectively, which can undergo secondary reactions to form alkylbenzenes. Another possible route for aromatic (xylenes) formation is through disproportionation and cracking of the heavy aromatics (C₉) in the hydrocarbon pool intermediates originated from oligomerization, dehydration, and cyclization between olefins and oxygenates (i.e., the oxygenate-hydrocarbon pool mechanism) [19]. Other monoaromatic compounds, such as benzene and toluene were not detected in the organic extracts by our GC-MS analysis; one possible reason may be that these two compounds are present in low concentrations below the detection limit of the instrument. In support of this argument, Wang et al. [67] and Xiao and Varma [70] demonstrated that the formation of xylenes is more pronounced than that of benzene and toluene during the glycerol-to-aromatics conversion over solid acid catalysts (H-ZSM-5), but the reasons for this observation remain unclear. Moreover, it is also likely that toluene reacts with C₉ aromatics, such as trimethylbenzenes to give xylenes through transalkylation [71], and thus both compounds were not observed in the product.

Once formed, the xylene vapors could be adsorbed on the catalyst surface, that is, via interactions between the methyl groups and the acid sites in HMMT, due to the strong affinity of the latter for this aromatic hydrocarbon [72,73]. The formed xylenes could condense with C₂-C₄ olefins similar to that observed in the hydrocarbon cracking [18], leading to coke formation that covers the acidic active sites. The compound A2 is thought to have formed by a consecutive aldol condensation of ketone to mesitylene, followed by cyclization and alkylation reactions. After 5 h TOS, the xylene peak at ~4.5 min was greatly diminished and the 1-hydroxycyclohexyl phenyl ketone (A3) peak at a retention time of ~11.7 min appeared. This latter compound might arise from cross-aldol condensation between the secondary reaction products of acetaldehyde and acetone. Although, at present, it is unclear whether the formation of 1-hydroxycyclohexyl phenyl ketone may involve reactions with xylenes, we reasoned that a diminishing xylene peak at longer TOS is plausibly attributed to the transformation of this compound to polycyclic aromatic species (insoluble coke) through condensation.

The aliphatic hydrocarbon compounds in soluble coke consist primarily of alkanes having twelve carbon atoms or longer. In this regard, the long-chain alkanes with carbon atoms equal to or greater than 18 units (i.e., peaks B6 and B7) could not be clearly defined, due to their characteristic peaks are very close to those having less carbon atoms. For TOS of 1 and 3 h, there are only minor changes in the hydrocarbon distributions (see Table 1). However, after 5 h of TOS, the relative abundances of dodecane (C₁₂H₂₆, peak B1) and pentadecane (C₁₅H₃₂, peak B2) decreased, while those of higher paraffins (C_mH_{2m+2}, peak B7) increased accordingly. Based on this observation, it can be deduced that the shorter-chain paraffins grow into longer-chain ones as the reaction progresses. There are two possible mechanisms for the formation of long-chain paraffins. The first one is the Fischer-Tropsch process from synthesis gas (CO and H₂). This mechanism, however, does not appear to be the case in the present catalytic system, since no CO and H₂ gases were fed to the reactor and the operating conditions applied during glycerol oxydehydration do not favor carbon chain growth and thus formation of long-chain alkanes [74]. Although CO and H₂ can be generated in situ during glycerol dehydration process [18], that is, from glycerol decomposition (C₃H₈O₃ ↔ 4 H₂ + 3CO) and steam reforming of oxygenate products (C_xH_yO_z + (x-z)H₂O ↔ (y/2 + x-z)H₂ + xCO), the required temperature for these reactions (T > 500 °C) is considerably higher than the applied operating temperature. The Fischer-Tropsch

Table 1Composition and relative abundances of organic species in CCl_4 -extracted soluble coke with TOS determined by GC-MS analysis.

Compound (Peak label)	Formula	bp (°C)	Relative Content [†]		
			1 h	3 h	5 h
<i>Aromatic hydrocarbons</i>					
Xylenes (A1)	C_8H_{10}	133-144	0.64	0.67	0.13
2,4-di-tert-butylphenol (A2)	$\text{C}_{14}\text{H}_{22}\text{O}$	265	0.87	0.83	0.87
1-Hydroxycyclohexyl phenyl ketone (A3)	$\text{C}_{13}\text{H}_{16}\text{O}_2$	339	–	0.02	0.68
<i>Aliphatic hydrocarbons</i>					
Dodecane (B1)	$\text{C}_{12}\text{H}_{26}$	216.3	0.79	0.76	0.55
Pentadecane (B2)	$\text{C}_{15}\text{H}_{32}$	270.6	0.92	0.85	0.75
Hexadecane (B3)	$\text{C}_{16}\text{H}_{34}$	286.9	1.00	1.00	1.00
Octadecane (B4)	$\text{C}_{18}\text{H}_{38}$	316.0	0.44	0.44	0.43
2,6,10,14-Tetramethylhexadecane (B5)	$\text{C}_{20}\text{H}_{42}$	322.9	0.60	0.54	0.64
$\text{C}_n\text{H}_{2n+2}$ ($n > 18$) (B6)	–	–	0.59	0.55	0.60
$\text{C}_m\text{H}_{2m+2}$ ($m > 18$) (B7)	–	–	0.15	0.15	0.29

[†]Relative abundance = $\frac{\text{peak area of A}_x\text{ or B}_y}{\text{peak area of B}_3}$

process can thus be ruled out as the operative mechanism of long-chain paraffin formation based on the above arguments.

Considering that glycerol molecules can oligomerize to form linear polyglycerols through intermolecular dehydration over acid sites [75],

we deduce that this is the likely pathway for the formation of paraffinic compounds in soluble coke. Coincidentally, the $\text{C}_x\text{H}_{2x+2}$ formula of linear oligoglycerols (i.e., $\text{C}_{12}\text{H}_{26}\text{O}_9$, $\text{C}_{15}\text{H}_{32}\text{O}_{11}$, and $\text{C}_{18}\text{H}_{38}\text{O}_{13}$ for tetra-, penta-, and hexaglycerol, respectively) matches exactly the

chemical formula of normal paraffins with the same carbon number detected in the extracts, suggesting that these two compounds are strongly interrelated. The formed polyglycerols may then undergo deoxygenation to produce linear alkanes, which is hypothesized to operate through a similar mechanism for deoxygenation of ethers to

form sp^3-sp^3 C–C bonds [76].

3.3.2. Insoluble coke

The chemical nature of insoluble coke deposited on the Mo-V/HMMT catalyst surface after 1, 3, and 5 h on stream was probed by ^{13}C solid-

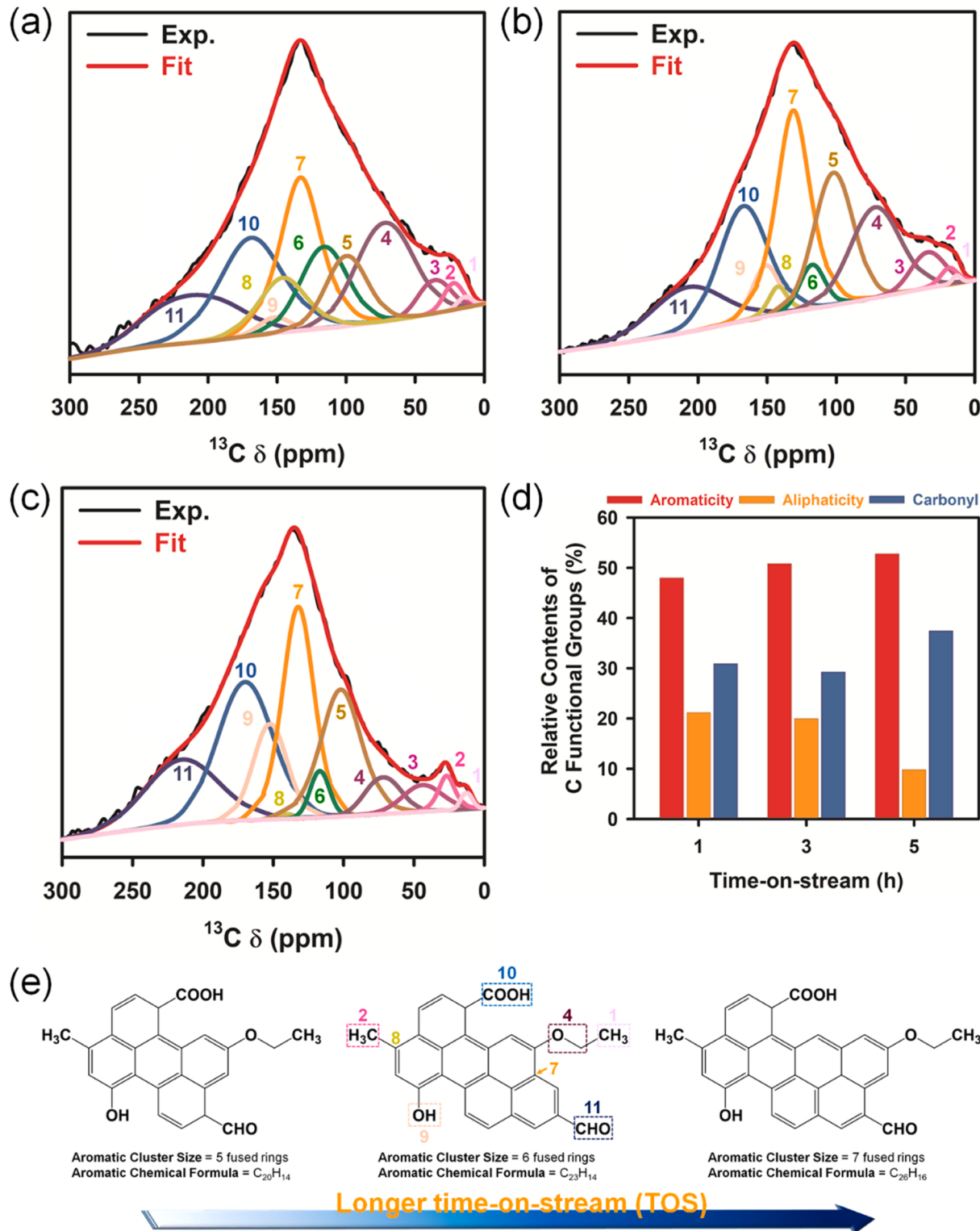


Fig. 6. ^{13}C solid-state MAS NMR spectra of insoluble coke deposits on spent Mo-V/HMMT catalysts after (a) 1, (b) 3, and (c) 5 h TOS. Solid lines with different colors show the deconvoluted individual peaks. (d) Relative contents (%) of different carbon functional groups. (e) Deduced chemical structure of insoluble cokes and their growth into larger aromatic clusters with TOS. Numbers in the middle chemical structure denote various types of carbon functional groups (for details see Table S4) based on the curve fitting of the ^{13}C NMR spectra.

state MAS NMR spectroscopy and the results are shown in Fig. 6a-c. As can be seen, the carbon spectral envelopes of the coked Mo-V/HMMT particles were very broad, indicating a highly heterogeneous nature of bulky insoluble coke compound as a result of the complex chemistries involved during its formation. As previously demonstrated for complex carbonaceous solids [25,31], the ^{13}C MAS NMR spectra of insoluble coke were deconvoluted into multiple peaks corresponding to various types of aromatic and aliphatic carbon compounds. The types of carbon functional groups can be inferred from the δ regions as follows: 0–50 ppm: alkyl C; 50–90 ppm: O-alkyl (alkoxy) C; 90–165 ppm: aromatic C; 165–190 ppm: carboxyl C; and 190–220 ppm: carbonyl C. The aromatic carbon signals can be further subdivided into several groups, including protonated (f_a^H) and bridgehead (f_a^B) aromatic carbons at 100–135 ppm, alkyl-substituted aromatic carbons (f_a^S) at 135–150 ppm, and phenolic carbons (f_a^P) at 150–165 ppm. The interpretation of the carbon resonance bands and their δ values for the spent Mo-V/HMMT catalysts at different TOS values are given in Table S4, in good agreement with previous literature reports [25,31,77].

Regardless of the TOS, the carbon resonance of insoluble coke all shows centers-of-mass at \sim 130 ppm, which falls in the sp^2 carbon region (110–160 ppm) and indicates the dominant aromaticity of the carbon deposits. Taking spent Mo-V/HMMT catalyst at a TOS of 1 h for example (Fig. 6a), various carbon resonance bands assignable to aliphatic CH_3 (δ = 13.2 ppm), aromatic CH_3 (δ = 21.8 ppm), methylene (δ = 34.9 ppm), oxymethylene (δ = 71.1 ppm), protonated aromatic (δ = 100.7 and 115.6 ppm), aromatic bridgehead (δ = 132.9 ppm), alkylated aromatic (δ = 145.3 ppm), hydroxybenzene (δ = 150.9 ppm), carboxyl (δ = 168.1 ppm), and carbonyl (δ = 208.0 ppm) were observed. The same resonance bands were seen in the ^{13}C NMR spectra of spent catalysts collected at 3 and 5 h on stream, suggesting that the chemical structure motif of insoluble coke changes. The relative contents of aliphatic, aromatic, and carbonyl carbons in the insoluble coke were determined from the ratio of the integrated peak area of these groups to the total peak area and their distributions with TOS are shown in Fig. 6d. At longer TOS, the aliphatic carbon spectral contributions in the range of 0–90 ppm (that is, peaks 1–4 in the NMR spectra) decrease, while those of aromatic carbon bands increase (peaks 5–9), indicative of the progressive aromatization of insoluble coke species as the reaction progresses and this is in line with the Raman spectroscopy results (Figure S21d).

An important structural information, that is, the fraction of aromatic carbon in bridgehead positions (χ_b), can be obtained from the ^{13}C NMR spectra. Specifically, the value of χ_b estimates the average number of carbon atoms (C#) in the aromatic cluster, as described in the work of Solum et al. [77]. As illustrated in Fig. 6e, the insoluble coke deposited on the Mo/V-HMMT catalyst surface at a TOS of 1 h possesses an aromatic cluster size of five fused-benzene rings containing 20 carbons (χ_b = 0.40) and the cluster size grows to average sizes of fused six (χ_b = 0.47) and seven benzene rings (χ_b = 0.52) for TOS of 3 and 5 h, respectively. The polycyclic aromatic compounds in the insoluble coke also contained different carbon functional groups, including methyl ($-\text{CH}_3$), methoxy ($-\text{OCH}_3$), carboxyl ($-\text{COOH}$), carbonyl ($-\text{CHO}$), and phenolic hydroxyl ($-\text{OH}$). Previous studies reported that polyglycerol-like coke deposits formed over acid zeolite catalysts exhibited carbon resonance bands at δ values of 63, 72, and 77 ppm [23, 29,78]. In the present case, the ^{13}C signals for polyglycerol are not resolved because of the broad features of the carbon spectral band containing prominent aromatic signals. Moreover, in those previous studies, the ^{13}C MAS NMR analyses of coked catalysts were carried out without separating soluble coke components from bulk carbon deposits. Furthermore, as has been described earlier, the glycerol oligomers are thought to be the precursor to long-chain paraffins, which are liberated from the bulk coke during CCl_4 extraction. This could in part explain why the polyglycerol carbon signals were not observed or they are supposed to be absent in the ^{13}C NMR spectra.

To further elucidate the nature of insoluble coke and shed light into

its temporal evolution during the reaction, the spent catalyst materials were examined by XPS. The high-resolution C 1 s and O 1 s XPS spectra for spent catalyst samples collected at 1, 3, and 5 h TOS were investigated to study the temporal distribution of different surface carbon species in insoluble coke. Here, the Al 2p peak at 74.2 eV was employed instead of traditional adventitious C 1 s peak for calibrating the binding energy (BE) scale, due to the reliability issue with using the latter for charge referencing as recently described in the work of Greczynski and Hultman [79]. As depicted in Fig. 7a, the survey spectra of spent Mo-V/HMMT catalysts exhibited carbon signal, which was absent in the as-prepared catalyst. In addition to the C 1 s peak at 284.2 eV, the constituent elements of the catalysts, such as Al, Si, Mo, and O were detected at BEs of 74.2, 102.2, 234.2, and 531.8 eV, respectively. With TOS, the surface concentrations of these elements decreased (Fig. 7b) and the Mo 3d peak vanished at 5 h TOS (Figure S26). These results, together with the increase in surface C concentration, indicate that the catalyst surface was covered by a greater amount of coke.

To reveal the detailed content of insoluble coke from XPS, the C 1 s region was fitted with a set of component peaks corresponding to different carbon hybridizations and carbon–oxygen functional groups. The results are presented in Table 2 and in good agreement with the BE values reported in the literature [80–84]. An overlay of the C 1 s XPS spectra (Fig. 7c) shows that the carbon signal at 5 h on stream is stronger and exhibits a broader tail spanning from 284.5 to 286.7 eV compared to those at shorter TOS (1 and 3 h). From Fig. 7d-f, it can be seen that the main peak of the C 1 s region can be well fitted by a single band at 284.2 eV assignable to sp^2 -hybridized carbon, hence suggesting the predominant aromatic nature of insoluble coke. A broad shoulder on the high BE side of the C 1 s envelope contains contributions from sp^3 -hybridized carbon at 285.6 eV and different types of oxygen-containing carbon species, such as C–OH (286.4 eV), C–O–C (287.1 eV), C=O (288.0 eV), and O=C=O (289.2 eV). The presence of oxygen bonded carbon species agrees with the experimental ^{13}C MAS NMR observations. With increasing TOS, the sp^2 surface concentration slightly decreased from 55.12 to 54.46%, while that of sp^3 bonded carbon increased from 21.32 to 29.88%. This may suggest that, at longer TOS, polycyclic coke deposits seem to become more alkylated.

3.4. Proposed formation mechanisms of soluble and insoluble cokes

On the basis of the coke characterization studies on soluble and insoluble fractions described above, we have attempted to depict two potential pathways for the formation of carbon deposits during the catalytic gas-phase oxydehydration of glycerol over Mo-V/HMMT catalyst, as illustrated in Fig. 8. As can be seen from this figure, the first pathway of coke formation involves the formation of aliphatic hydrocarbons derived from linear oligoglycerol molecules. When the number of carbons in the aliphatic hydrocarbons increases to 12 or more, they are likely to be deposited on the surface of the catalyst. Then, the chain length of the aliphatic hydrocarbons will continually increase and the long-chain aliphatic hydrocarbons are formed. The second pathway of coking involves aldol condensation of carbonyl-containing compounds, such as acetaldehyde, propionaldehyde, acetone, and others in the catalytic oxydehydration of glycerol. These carbonyl-containing compounds can undergo aldol condensation to generate monoaromatic species, such as xylene, 2,4-di-tert-butylphenol, and 1-hydroxycyclohexyl phenyl ketone. With TOS, these deposited mono-nuclear aromatic derivatives continue to form fused-ring polycyclic aromatic molecules bearing various functional groups, such as methyl, carboxyl, carbonyl, and phenolic hydroxyl groups.

3.5. Implications for catalyst design

Mo-V based oxide catalyst materials have been widely studied for gas-phase selective conversion of glycerol to acrolein and/or acrylic acid, and while coke formation within the catalyst particles is inevitable

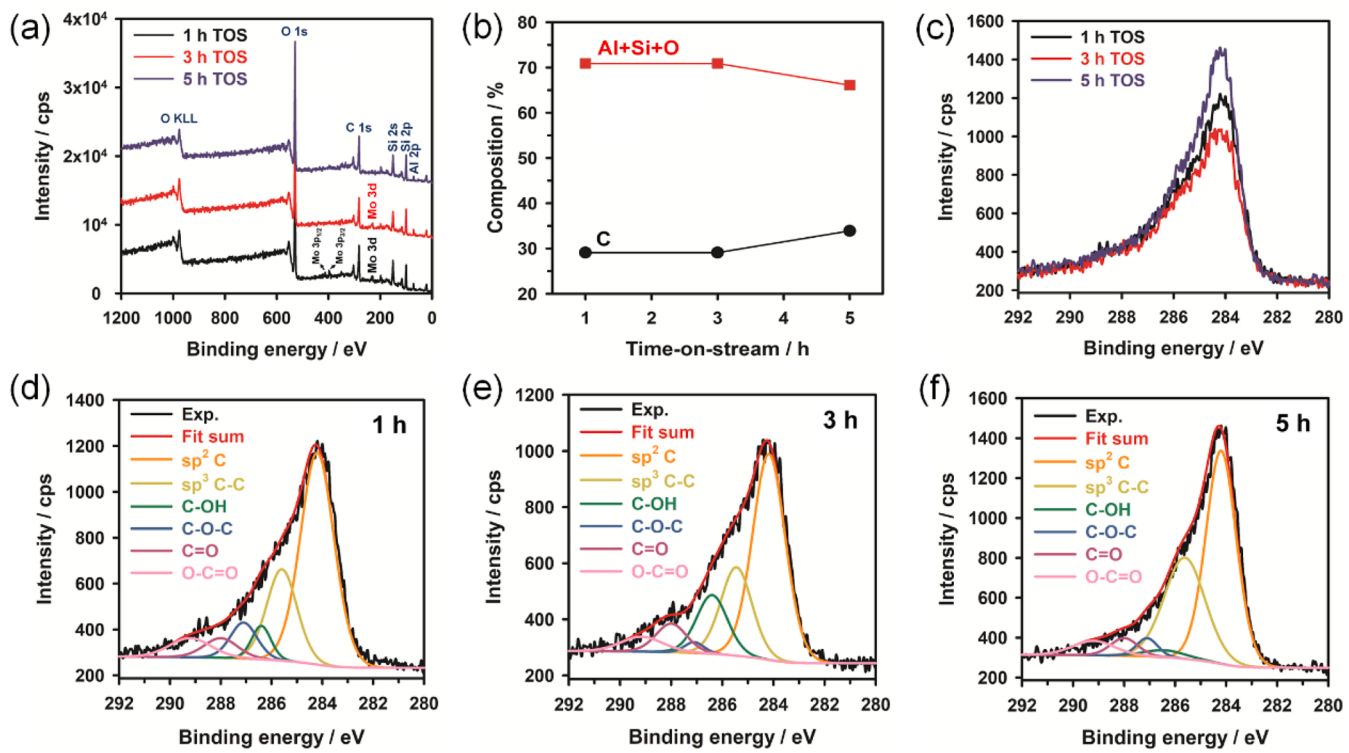


Fig. 7. (a) XPS survey spectra, (b) surface composition, and (c) overlay and (d-f) high-resolution C 1 s XPS spectra of insoluble coke deposits on spent Mo-V/HMMT catalysts at TOS of 1, 3, and 5 h. All binding energies were referenced to the Al 2p peak at 74.2 eV and reported ± 0.1 eV.

Table 2

Relative atomic concentrations of various surface carbon species of insoluble coke obtained from the curve fitting of the C 1 s XPS spectra of spent Mo-V/HMMT catalysts as a function of TOS.

TOS (h)	Functional Groups / Atomic					
	sp ² C (284.2)	sp ³ C-C (285.6)	C-OH (286.4)	C-O-C (287.1)	C=O (288.0)	O-C=O (289.2)
1	55.12	21.32	4.96	7.39	5.08	6.13
3	54.83	21.28	9.92	2.58	5.67	5.72
5	54.46	29.88	2.44	3.90	3.87	5.45

during this catalytic process, at present there is not much information regarding the catalyst design approaches to minimize coking level. Here, using HMMT-supported Mo-V-O as a model catalytic solid, we provide insights into the coking behavior of the catalyst materials and ways to design improved coke-resistant catalysts. First, our results show that the incorporation of well-dispersed amorphous Mo-V-O species resulted in diminution of the HMMT support acidity by decreasing the total amount and strength of the acid sites, thus leading to lower deactivation and coking rates of the catalysts. Second, the metal composition–coking relationship study, including supported monometal catalysts (i.e., Mo/HMMT and V/HMMT), suggests that Mo and V contribute synergistically to the enhanced coking resistance and reduced deactivation of the Mo-V/HMMT catalysts. In particular, the modulation of Mo/(Mo+V) mole ratio during impregnation of the HMMT support shows that

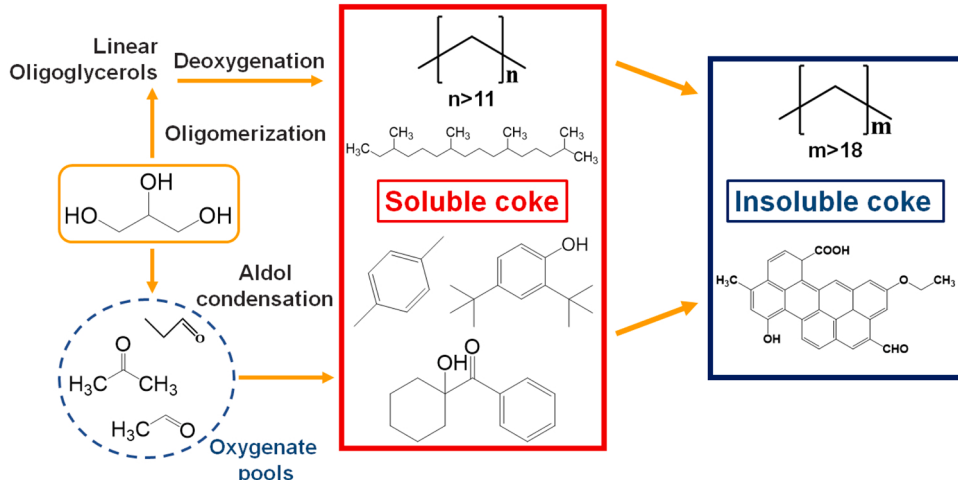


Fig. 8. Proposed modes of coke formation during gas-phase glycerol oxydehydration process over Mo-V/HMMT catalyst.

increasing the proportion of Mo improves the Mo-V/HMMT catalyst activity through generation of new strong acid sites with Brønsted character, but this also concomitantly promotes coke formation. The XPS analysis suggests that the presence of adequate Mo(VI) species, which exhibit strong electronic interactions with the support, could help reduce the propensity of catalyst to coking, as well as enhance the initial catalytic activity. With regard to V, a higher proportion of V^{4+} species on the Mo-V/HMMT catalyst surface is not necessarily beneficial for coking resistance but it may facilitate the formation of less deactivating 'softer' coke deposits. Therefore, the modulation of Mo and V compositional ratios in the supported Mo-V-O catalysts should consider a good compromise between activity and the extent of deactivation. Lastly, the deactivating effect of carbon deposits formed on the catalyst depends on the pore structure, including size and shape. Within this context, the solid acid catalysts possessing interconnected micro-meso (large) slit-pore structure are supposed to show enhanced coking resistance and less detrimental coke-deactivating effect. Regarding micropores, we reasoned that the pore width should be large enough (that is, in the range of 0.7 to 1.5 nm) to allow for facile access of glycerol molecules to the internal active sites and diffusion of the formed coke precursor compounds out of the catalyst interior, which could reduce the blockage of the pores by growing coke species and therefore prolong the catalyst lifetime. In addition, the creation of micropores hosting acid active sites of similar strength could lead to lower coking rate and consequently more stable catalyst activity during the early stages of the reaction.

4. Conclusion

The present study investigates the chemical aspects of coking of HMMT-supported Mo-V-O catalysts with different Mo/(Mo+V) compositional ratios during gas-phase oxydehydration of glycerol. The loaded Mo-V species by impregnation were well dispersed on the support surface, as confirmed by both XRD and Raman spectroscopy, and the existence of metal-support interaction, typically with Al atoms in the octahedral sheet, was revealed by FTIR spectroscopy. The TOS tests of the Mo-V/HMMT catalysts (Mo/(Mo+V) ratio = 0.8) show that, although coke formation was observed in the early stage (within the first hour) of the reaction, this material was able to achieve high initial catalytic activity in terms of conversion and acrolein selectivity. At a later stage of TOS, the progressive coke formation causes significant deactivation of the catalyst, probably due to the blockage of micro- and/or small mesopores of the catalyst. Calcination of coked Mo-V/HMMT catalysts at 500 °C could remove nearly all amorphous carbon deposits and thereby restores the catalytic activity. The possible contribution of the coke deposits to the catalytic process, that is, by serving as a hydrogen donor in the hydrogen transfer reaction of acrolein to allyl alcohol (the second most abundant product detected in the condensate) is pointed out in the present catalyst system, although this remains speculative, but plausible, and requires further research to clarify.

Post-mortem characterizations of coked Mo-V/HMMT catalysts at different TOS, including the extraction of soluble components from the bulk of coke deposits formed enable the elucidation of their chemical nature and the corresponding coke formation mechanism. While the structure of coke deposits remains predominantly amorphous, the composition of coke-forming constituents changes with TOS. Soluble cokes were composed of mononuclear aromatic derivatives and long-chain paraffins, whereas the insoluble fractions were comprised of polycyclic aromatic molecules with 5 or more fused-benzene rings and containing heterogeneous functional groups, such as $-\text{CH}_3$, $-\text{OCH}_3$, $-\text{OH}$, $-\text{CHO}$, and $-\text{COOH}$. Thorough characterization of the chemical nature of coke provide hints to the two potential pathways for coking of Mo-V/HMMT catalyst in the gas-phase oxydehydration of glycerol. The aliphatic hydrocarbons may be formed from linear oligoglycerols through deoxygenation. The carbon chain length of the aliphatic hydrocarbons grows with TOS. In the second route, the aldol condensation of acetaldehyde, propanal, or acetone may lead to the formation of the

mononuclear aromatic derivatives, such as xylene, 2,4-di-tert-butylphenol and 1-hydroxycyclohexyl phenyl ketone. These aromatic derivatives are converted into the fused-ring polycyclic aromatic derivatives with diverse functional groups. Hence, limiting the extents of glycerol oligomerization and aldol condensation reactions during gas-phase oxydehydration of glycerol may contribute to reduced deposition of coke on the catalyst. In summary, this work presents insights to better understand the nature and formation pathways of coke on supported Mo-V-O catalysts in the industrially important gas-phase glycerol oxydehydration process, which could pave the way for designing improved coke-resistant materials.

CRediT authorship contribution statement

Li Ke Jin: Data curation, Writing – original draft. **Chen Xiao Lan:** Visualization. **Yin Shu Tian:** Investigation. **Li Da Jian:** Investigation. **Kurniawan Alfin:** Data curation, Investigation, Methodology, Writing – original draft, Writing – review & editing. **Liu Jia Hui:** Visualization. **Zhou Chun-Hui:** Conceptualization, Funding acquisition, Project administration, Supervision, Writing – review & editing. **Huang Wei Jun:** Data curation, Formal analysis, Writing – original draft. **Zhao Peng Yang:** Visualization.

Declaration of Competing Interest

The authors declare that they have no known competing financial interests or personal relationships that could have appeared to influence the work reported in this paper.

Data Availability

Data will be made available on request.

Acknowledgements

The authors wish to acknowledge the financial support from the National Natural Science Foundation of China (22072136; 41672033), the Engineering Research Center of Non-metallic Minerals of Zhejiang Province (ZD2023K01), and the Qing Yang Institute for Industrial Minerals (KYY-HX-20220336; KYY-HX-20170557).

Appendix A. Supporting information

Supplementary data associated with this article can be found in the online version at [doi:10.1016/j.apcatb.2024.123766](https://doi.org/10.1016/j.apcatb.2024.123766).

References

- [1] Statista Research Department, 2022, FAME biodiesel production volume worldwide from 2014 to 2021. Global FAME biodiesel production 2021 | Statista (accessed 2023-02-10).
- [2] G.M. Lari, G. Pastore, M. Haus, Y.Y. Ding, S. Papadokonstantakis, C. Mondelli, J. Perez-Ramirez, Environmental and economical perspectives of a glycerol biorefinery, *Energy Environ. Sci.* 11 (2018) 1012–1029.
- [3] S. Xu, Q. Tian, Y. Xiao, W. Zhang, S. Liao, J. Li, C. Hu, Regulating the competitive reaction pathway in glycerol conversion to lactic acid/glycolic acid selectively, *J. Catal.* 413 (2022) 407–416.
- [4] S. Liu, Z. Yu, C. Lu, Y. Wang, F. Sun, Z. Sun, Y. Liu, C. Shi, A. Wang, Copper carbide composite catalyst for hydrogenolysis of glycerol to 1,2-propanediol, *Fuel* 334 (Part 2) (2023) 126723.
- [5] J. Shan, Z. Li, Z. Chen, D. Wang, X. Zhang, Z. Ning, Y. Xue, S. Zhu, Enhancement in catalytic performance of HZSM-5 zeolite for glycerol dehydration after acidity regulation, *Chem. Eng. J.* 460 (2023) 141741.
- [6] E.Y. Mertsoy, E. Sert, S. Atalay, F.S. Atalay, Fabrication of chromium based metal organic framework (MIL-101)/activated carbon composites for glycerol, *J. Taiwan Inst. Chem. Eng.* 120 (2021) 93–105.
- [7] D.L. Sun, Y. Yamada, S. Sato, W. Ueda, Glycerol as a potential renewable raw material for acrylic acid production, *Green. Chem.* 19 (2017) 3186–3213.
- [8] J. Deleplanque, J.-L. Dubois, J.-F. Devaux, W. Ueda, Production of acrolein and acrylic acid through dehydration and oxydehydration of glycerol with mixed oxide catalysts, *Catal. Today* 157 (2010) 351–358.

[9] S. Ishikawa, Y. Yamada, C. Qiu, Y. Kawahara, N. Hiyoshi, A. Yoshida, W. Ueda, Synthesis of a crystalline orthorhombic Mo–V–Cu oxide for selective oxidation of acrolein, *Chem. Mater.* 31 (2019) 1408–1417.

[10] A. Chieregato, M.D. Soriano, F. Basile, G. Liosi, S. Zamora, P. Concepción, F. Cavani, J.M.L.ópez Nieto, One-pot glycerol oxidehydration to acrylic acid on multifunctional catalysts: Focus on the influence of the reaction parameters in respect to the catalytic performance, *Appl. Catal. B: Environ.* 150–151 (2014) 37–46.

[11] K. Omata, K. Matsumoto, T. Murayama, W. Ueda, Direct oxidative transformation of glycerol to acrylic acid over Nb-based complex metal oxide catalysts, *Catal. Today* 259 (Part 1) (2016) 205–212.

[12] W. Yu, P. Wang, C. Zhou, H. Zhao, D. Tong, H. Zhang, H. Yang, S. Ji, H. Wang, Acid-activated and WO_x -loaded montmorillonite catalysts and their catalytic behaviors in glycerol dehydration, *Chin. J. Catal.* 38 (2017) 1087–1100.

[13] V.V. Bokade, G.D. Yadav, Heteropolyacid supported on montmorillonite catalyst for dehydration of dilute bio-ethanol, *Appl. Clay Sci.* 53 (2011) 236–271.

[14] G.-Q. Huang, Y.-H. Song, C. Liu, J.-M. Yang, J. Lu, Z.-T. Liu, Z.-W. Liu, Acid activated montmorillonite for gas-phase catalytic dehydration of monoethanolamine, *Appl. Clay Sci.* 168 (2019) 116–124.

[15] M. Guisnet, L. Costa, F.R. Ribeiro, Prevention of zeolite deactivation by coking, *J. Mol. Catal. A-Chem.* 305 (2009) 69–83.

[16] L.G. Possato, R.N. Diniz, T. Garetto, S.H. Pulcinelli, C.V. Santilli, L. Martins, A comparative study of glycerol dehydration catalyzed by micro/mesoporous MFI zeolites, *J. Catal.* 300 (2013) 102–112.

[17] W. Suprun, M. Lutecki, T. Haber, H. Papp, Acidic catalysts for the dehydration of glycerol: activity and deactivation, *J. Mol. Catal. A-Chem.* 309 (2009) 71–78.

[18] A. Corma, G.W. Huber, L. Sauvanaud, P. O'Connor, Biomass to chemicals: catalytic conversion of glycerol/water mixtures into acrolein, reaction network, *J. Catal.* 257 (2008) 163–171.

[19] S. Tamiyakul, W. Ubolcharoen, D.N. Tungasmita, S. Jongpatiwut, Conversion of glycerol to aromatic hydrocarbons over Zn-promoted HZSM-5 catalysts, *Catal. Today* 256 (2015) 325–335.

[20] J. Barrault, J.-M. Clacens, Y. Pouilloux, Selective oligomerization of glycerol over mesoporous catalysts, *Top. Catal.* 27 (2004) 137–142.

[21] X.C. Jiang, C.H. Zhou, R. Tesser, M. Di Serio, D.S. Tong, J.R. Zhang, Coking of catalysts in catalytic glycerol dehydration to acrolein, *Ind. Eng. Chem. Res.* 57 (2018) 10736–10753.

[22] Y.T. Kim, K.-D. Jung, E.D. Park, Gas-phase dehydration of glycerol over silica–alumina catalysts, *Appl. Catal. B: Environ.* 107 (2011) 177–187.

[23] L.H. Vieira, K.T.G. Carvalho, E.A. Urquiza-González, S.H. Pulcinelli, C.V. Santilli, L. Martins, Effects of crystal size, acidity, and synthesis procedure on the catalytic performance of gallium and aluminum MFI zeolites in glycerol dehydration, *J. Mol. Catal. A-Chem.* 422 (2016) 148–157.

[24] S.-H. Chai, H.-P. Wang, Y. Liang, B.-Q. Xu, Sustainable production of acrolein: gas-phase dehydration of glycerol over Nb_2O_5 catalyst, *J. Catal.* 250 (2007) 342–349.

[25] N. Wang, Y. Zhi, Y. Wei, W. Zhang, Z. Liu, J. Huang, T. Sun, S. Xu, S. Lin, Y. He, A. Zheng, Z. Liu, Molecular elucidating of an unusual growth mechanism for polycyclic aromatic hydrocarbons in confined space, *Nat. Commun.* 11 (2020) 1079.

[26] L. Emdadi, L. Mahoney, I.C. Lee, A.C. Leff, W. Wu, D. Liu, C.K. Nguyen, D.T. Tran, Assessment of coke deposits on lamellar metal-modified MFI zeolites in ethylene transformation to aromatic liquids, *Appl. Catal. A, Gen.* 595 (2020) 117510.

[27] J. Goetze, I. Yarulina, J. Gascon, F. Kapteijn, B.M. Weckhuysen, Revealing lattice expansion of small-pore zeolite catalysts during the methanol-to-olefins process using combined operando X-ray diffraction and UV-vis spectroscopy, *ACS Catal.* 8 (2018) 2060–2070.

[28] P.C. Stair, The application of UV Raman spectroscopy for the characterization of catalysts and catalytic reactions, *Adv. Catal.* 51 (2007) 75–98.

[29] L.G. Possato, W.H. Cassinelli, T. Garetto, S.H. Pulcinelli, C.V. Santilli, L. Martins, One-step glycerol oxidehydration to acrylic acid on multifunctional zeolite catalysts, *Appl. Catal. A: Gen.* 492 (2015) 243–251.

[30] W. Yu, P. Wang, C. Zhou, H. Zhao, D. Tong, H. Zhang, H. Yang, S. Ji, H. Wang, Acid-activated and WO_x -loaded montmorillonite catalysts and their catalytic behaviors in glycerol dehydration, *Chin. J. Catal.* 38 (2017) 1087–1100.

[31] Y.-G. Wang, X.-Y. Wei, R.-L. Xie, F.-J. Liu, P. Li, Z.-M. Zong, Structural characterization of typical organic species in Jincheng No. 15 anthracite, *Energy Fuels* 29 (2015) 595–601.

[32] L. Zatta, L.P. Ramos, F. Wypych, Acid-activated montmorillonites as heterogeneous catalysts for the esterification of lauric acid with methanol, *Appl. Clay Sci.* 80–81 (2013) 236–244.

[33] S.E. Kelch, E. Ferrage, B. Lanson, L. Charlet, L. Aristilde, Water trapping dynamics in carbohydrate-populated smectite interlayer nanopores, *J. Phys. Chem. C* 123 (2019) 28816–28827.

[34] J. Kielland, Individual activity coefficients of ions in aqueous solutions, *J. Am. Chem. Soc.* 59 (1937) 1675–1678.

[35] E. Ferrage, B. Lanson, L.J. Michot, J.-L. Robert, Hydration properties and interlayer organization of water and ions in synthetic Na-smectite with tetrahedral layer charge. Part 1. Results from X-ray diffraction profile modeling, *J. Phys. Chem. C* 114 (2010) 4515–4526.

[36] J.H. Kwak, J. Hu, D. Mei, C.-W. Yi, D.H. Kim, C.H.F. Peden, L.F. Allard, J. Szanyi, Coordinatively unsaturated Al^{3+} centers as binding sites for active catalyst phases of platinum on $\gamma\text{-Al}_2\text{O}_3$, *Science* 325 (2009) 1670–1673.

[37] J. Madejová, FTIR techniques in clay mineral studies, *Vib. Spectrosc.* 31 (2003) 1–10.

[38] R. Obunai, K. Tamura, I. Ogino, S.R. Mukai, W. Ueda, Mo–V–O nanocrystals synthesized in the confined space of a mesoporous carbon, *Appl. Catal. A, Gen.* 624 (2021) 118294.

[39] L. Seguin, M. Figlarz, R. Cavagnat, J.-C. Lassegues, Infrared and Raman spectra of MoO_3 molybdenum trioxides and $\text{MoO}_3\text{-xH}_2\text{O}$ molybdenum trioxide hydrates, *Spectrochim. Acta Part A* 51 (1995) 1323–1344.

[40] N. Magg, B. Immaraporn, J.B. Giorgi, T. Schroeder, M. Bäumer, J. Döbler, Z. Wu, E. Kondratenko, M. Cherian, M. Baerns, P.C. Stair, J. Sauer, H.-J. Freund, Vibrational spectra of alumina- and silica-supported vanadia revisited: an experimental and theoretical model catalyst study, *J. Catal.* 226 (2004) 88–100.

[41] T. Hirata, In-situ observation of Mo–O stretching vibrations during the reduction of MoO_3 with hydrogen by diffuse reflectance FTIR spectroscopy, *Appl. Surf. Sci.* 40 (1989) 179–181.

[42] L. Pinard, S. Hamieh, C. Canaff, F. Ferreira, Growth mechanism of coke on HBEA zeolite during ethanol transformation, *J. Catal.* 299 (2013) 284–297.

[43] L. Palumbo, F. Bonino, P. Beato, M. Bjørgen, A. Zecchina, S. Bordiga, Conversion of methanol to hydrocarbons: Spectroscopic characterization of carbonaceous species formed over H-ZSM-5, *J. Phys. Chem. C* 112 (2008) 9710–9716.

[44] Y.V. Plyuto, I.V. Babich, I.V. Plyuto, A.D. Van Langeveld, J.A. Mouljin, XPS studies of $\text{MoO}_3/\text{Al}_2\text{O}_3$ and $\text{MoO}_3/\text{SiO}_2$ systems, *Appl. Surf. Sci.* 119 (1997) 11–18.

[45] S. Chen, L. Zeng, R. Mu, C. Xiong, Z.-J. Zhao, C. Zhao, C. Pei, L. Peng, J. Luo, L.-S. Fan, J. Gong, Modulating lattice oxygen in dual-functional Mo–V–O mixed oxides for chemical looping oxidative dehydrogenation, *J. Am. Chem. Soc.* 141 (2019) 18653–18657.

[46] F. Klose, T. Wolff, H. Lorenz, A. Seidel-Morgenstern, Y. Suchorski, M. Piórkowska, H. Weiss, Active species on γ -alumina-supported vanadia catalysts: nature and reducibility, *J. Catal.* 247 (2007) 176–193.

[47] X. Feng, Y. Yao, Q. Su, L. Zhao, W. Jiang, W. Ji, C.-T. Au, Vanadium pyrophosphate oxides: the role of preparation chemistry in determining renewable acrolein production from glycerol dehydration, *Appl. Catal. B: Environ.* 164 (2015) 31–39.

[48] P. Shvets, O. Dikaya, K. Maksimova, A. Goikhman, A review of Raman spectroscopy of vanadium oxides, *J. Raman Spectrosc.* 50 (2019) 1226–1244.

[49] M. Ritz, L. Vaculíková, J. Kupková, E. Plevová, L. Bartoňová, Different level of fluorescence in Raman spectra of montmorillonites, *Vib. Spectrosc.* 84 (2016) 7–15.

[50] M.H. Haider, C. D'Agostino, N.F. Dummer, M.D. Mantle, L.F. Gladden, D. W. Knight, D.J. Willcock, D.J. Morgan, S.H. Taylor, G.J. Hutchings, The effect of grafting zirconia and ceria onto alumina as a support for silicotungstic acid for the catalytic dehydration of glycerol to acrolein, *Chem.: A Eur. J.* 20 (2014) 1743–1752.

[51] J.A. Cecilia, C. García-Sancho, J.M. Mérida-Robles, J. Santamaría-González, R. Moreno-Tost, P. Maireles-Torres, V and VP containing Zr-SBA-15 catalysts for dehydration of glycerol to acrolein, *Catal. Today* 254 (2015) 43–52.

[52] B. Viswanadham, A. Srikanth, V.P. Kumar, K.V.R. Chary, Vapor phase dehydration of glycerol to acrolein over SBA-15 supported vanadium substituted phosphomolybdc acid catalyst, *J. Nanosci. Nanotechnol.* 15 (2015) 5391–5402.

[53] A.S. Belousov, A.L. Esiopovich, K.V. Otopokova, E.A. Kanakov, V.D. Uvarova, A. V. Shishulina, A.V. Vorotynsev, Ga-phase dehydration of glycerol into acrolein in the presence of polyoxometalates, *Kinet. Catal.* 61 (2020) 595–602.

[54] Y. Liu, H. Tüysüz, C.-J. Jia, M. Schwickardi, R. Rinaldi, A.-H. Lu, W. Schmidt, F. Schütt, From glycerol to allyl alcohol: iron oxide catalyzed dehydration and consecutive hydrogen transfer, *Chem. Commun.* 46 (2010) 1238–1240.

[55] L.R. Smith, P.J. Smith, K.S. Mugford, M. Douthwaite, N.F. Dummer, D.J. Willcock, M. Howard, D.W. Knight, S.H. Taylor, G.J. Hutchings, New insights for the valorisation of glycerol over MgO catalysts in the gas-phase, *Catal. Sci. Technol.* 9 (2019) 1464–1475.

[56] I. Hita, H.O. Mohamed, Y. Attada, N. Zambrano, W. Zhang, A. Ramírez, P. Castaño, Direct analysis at temporal and molecular level of deactivating coke species formed on zeolite catalysts with diverse pore topologies, *Catal. Sci. Technol.* 13 (2023) 1288–1300.

[57] A.C. Ferrari, Raman spectroscopy of graphene and graphite: disorder, electron–phonon coupling, doping and nonadiabatic effects, *Solid State Commun.* 143 (2007) 47–57.

[58] D. Lin-Vien, N.B. Colthup, W.G. Fateley, J.G. Grasselli, CHAPTER 17 - aromatic and heteroaromatic rings. *The Handbook of Infrared and Raman Characteristic Frequencies of Organic Molecules*, Academic Press, 1991, pp. 277–306.

[59] D. Lin-Vien, N.B. Colthup, W.G. Fateley, J.G. Grasselli, - Compounds containing the carbonyl group. *The Handbook of Infrared and Raman Characteristic Frequencies of Organic Molecules*, Academic Press, 1991, pp. 117–154.

[60] S. He, C. Sun, X. Yang, B. Wang, X. Dai, Z. Bai, Characterization of coke deposited on spent catalysts for long-chain-paraffin dehydrogenation, *Chem. Eng. J.* 163 (2010) 389–394.

[61] S. Müller, Y. Liu, M. Vishnuvarthan, X. Sun, A.C. van Veen, G.L. Haller, M. Sanchez-Sánchez, J.A. Lercher, Coke formation and deactivation pathways on H-ZSM-5 in the conversion of methanol to olefins, *J. Catal.* 325 (2015) 48–59.

[62] C.H. Collett, J. McGregor, Things go better with coke: the beneficial role of carbonaceous deposits in heterogeneous catalysis, *Catal. Sci. Technol.* 6 (2016) 363–378.

[63] M.E.Z. Velthoen, S. Nab, B.M. Weckhuysen, Probing acid sites in solid catalysts with pyridine UV-Vis spectroscopy, *Phys. Chem. Chem. Phys.* 20 (2018) 21647–21659.

[64] D. Liu, P. Yuan, H. Liu, J. Cai, D. Tan, H. He, J. Zhu, T. Chen, Quantitative characterization of the solid acidity of montmorillonite using combined FTIR and TPD based on the NH_3 adsorption system, *Appl. Clay Sci.* 81 (2013) 407–412.

[65] Y. Zhang, M. Li, E. Xing, Y. Luo, X. Shu, Coke evolution on mesoporous ZSM-5 during methanol to propylene reaction, *Catal. Commun.* 119 (2019) 67–70.

[66] X. Li, Y. Huang, Q. Zhang, C. Luan, V.A. Vinokurov, W. Huang, Highly stable and anti-coking Ni/MoCeZr/MgAl₂O₄-MgO complex support catalysts for CO₂ reforming of CH₄: Effect of the calcination temperature, *Energy Convers. Manag.* 179 (2019) 166–177.

[67] F. Wang, W. Xiao, L. Gao, G. Xiao, Enhanced performance of glycerol to aromatics over Sn-containing HZSM-5 zeolites, *RSC Adv.* 6 (2016) 42984–42993.

[68] T.Q. Hoang, X. Zhu, T. Danuthai, L.L. Lobban, D.E. Resasco, R.G. Mallinson, Conversion of glycerol to alkyl-aromatics over zeolites, *Energy Fuels* 24 (2010) 3804–3809.

[69] S. Luo, J.L. Falconer, Acetone and acetaldehyde oligomerization on TiO₂ surfaces, *J. Catal.* 185 (1999) 393–407.

[70] Y. Xiao, A. Varma, Conversion of glycerol to hydrocarbon fuels via bifunctional catalysts, *ACS Energy Lett.* 1 (2016) 963–968.

[71] T.-C. Tsai, S.-B. Liu, I. Wang, Disproportionation and transalkylation of alkylbenzenes over zeolite catalysts, *Appl. Catal. A: Gen.* 181 (1999) 355–398.

[72] Y.C. Li, G. Gupta, Adsorption of hydrocarbons by clay-minerals from gasoline, *J. Hazard. Mater.* 38 (1994) 105–112.

[73] H. Zaitan, D. Bianchi, O. Achak, T. Chafik, A comparative study of the adsorption and desorption of *o*-xylene onto bentonite clay and alumina, *J. Hazard. Mater.* 153 (2008) 852–859.

[74] G.P. Van Der Laan, A.A.C.M. Beenackers, Kinetics and selectivity of the Fischer–Tropsch synthesis: a literature review, *Catal. Rev.: Sci. Eng.* 41 (1999) 255–318.

[75] A. Martin, M. Richter, Oligomerization of glycerol – a critical review, *Eur. J. Lipid Sci. Technol.* 113 (2011) 100–117.

[76] Z.-C. Cao, Z.-J. Shi, Deoxygenation of ethers to form carbon–carbon bonds via nickel catalysis, *J. Am. Chem. Soc.* 139 (2017) 6546–6549.

[77] M.S. Solum, R.J. Pugmire, D.M. Grant, ¹³C solid-state NMR of Argonne premium coals, *Energy Fuels* 3 (1989) 187–193.

[78] M.V. Rodrigues, C. Vignatti, T. Garetto, S.H. Pulcinelli, C.V. Santilli, L. Martins, Glycerol dehydration catalyzed by MWW zeolites and the changes in the catalyst deactivation caused by porosity modification, *Appl. Catal. A: Gen.* 495 (2015) 84–91.

[79] G. Greczynski, L. Hultman, The same chemical state of carbon gives rise to two peaks in X-ray photoelectron spectroscopy, *Sci. Rep.* 11 (2021) 11195.

[80] P.-G. Ren, D.-X. Yan, X. Ji, T. Chen, Z.-M. Li, Temperature dependence of graphene oxide reduced by hydrazine hydrate, *Nanotechnology* 22 (2011) 055705.

[81] R. Pandiyan, N. Delegan, A. Dirany, P. Drogui, M.A. El Khakani, Correlation of sp² carbon bonds content in magnetron-sputtered amorphous carbon films to their electrochemical H₂O₂ production for water decontamination applications, *Carbon* 94 (2015) 988–995.

[82] Q. Dou, S. Lei, D.-W. Wang, Q. Zhang, D. Xiao, H. Guo, A. Wang, H. Yang, Y. Li, S. Shi, X. Yan, Safe and high-rate supercapacitors based on an "acetonitrile/water in salt" hybrid electrolyte, *Energy Environ. Sci.* 11 (2018) 3212–3219.

[83] F. Zhou, H.N. Tien, Q. Dong, W.L. Xu, B. Sengupta, S. Zha, J. Jiang, D. Behera, S. Li, M. Yu, Novel carbon-based separation membranes composed of integrated zero- and one-dimensional nanomaterials, *J. Mater. Chem. A* 8 (2020) 1084–1090.

[84] L. Stobinski, B. Lesiak, A. Malolepszy, M. Mazurkiewicz, B. Mierzwa, J. Zemek, P. Jiricek, I. Bieloshapka, Graphene oxide and reduced graphene oxide studied by the XRD, TEM and electron spectroscopy methods, *J. Electron Spectrosc. Relat. Phenom.* 195 (2014) 145–154.